INTERFACE

royalsocietypublishing.org/journal/rsif

Research

Cite this article: Jawde SB *et al*. 2021 Inflation instability in the lung: an analytical model of a thick-walled alveolus with wavy fibres under large deformations. *J. R. Soc. Interface* **18**: 20210594.
https://doi.org/10.1098/rsif.2021.0594

Received: 18 July 2021
Accepted: 9 September 2021

Subject Category:
Life Sciences–Mathematics interface

Subject Areas:
biomedical engineering, biomechanics, computational biology

Keywords:
mathematical model, Cauchy stress, stiffness, collagen, runaway phenomenon

Author for correspondence:
Béla Suki
e-mail: bsuki@bu.edu

Electronic supplementary material is available online at https://doi.org/10.6084/m9.figshare.c.5632617.

THE ROYAL SOCIETY PUBLISHING

Inflation instability in the lung: an analytical model of a thick-walled alveolus with wavy fibres under large deformations

Samer Bou Jawde[1], Kavon Karrobi[1], Darren Roblyer[1], Francesco Vicario[2], Jacob Herrmann[1], Dylan Casey[3], Kenneth R. Lutchen[1], Dimitrije Stamenović[1], Jason H. T. Bates[3] and Béla Suki[1]

[1]Department of Biomedical Engineering, Boston University, 44 Cummington Mall, Boston, MA 02215, USA
[2]Philips Research, Cambridge, MA, USA
[3]Pulmonary/Critical Care Division, University of Vermont, Burlington, VT, USA

JH, 0000-0001-5046-5592; BS, 0000-0002-9720-1006

Inflation of hollow elastic structures can become unstable and exhibit a runaway phenomenon if the tension in their walls does not rise rapidly enough with increasing volume. Biological systems avoid such inflation instability for reasons that remain poorly understood. This is best exemplified by the lung, which inflates over its functional volume range without instability. The goal of this study was to determine how the constituents of lung parenchyma determine tissue stresses that protect alveoli from instability-related overdistension during inflation. We present an analytical model of a thick-walled alveolus composed of wavy elastic fibres, and investigate its pressure–volume behaviour under large deformations. Using second-harmonic generation imaging, we found that collagen waviness follows a beta distribution. Using this distribution to fit human pressure–volume curves, we estimated collagen and elastin effective stiffnesses to be 1247 kPa and 18.3 kPa, respectively. Furthermore, we demonstrate that linearly elastic but wavy collagen fibres are sufficient to achieve inflation stability within the physiological pressure range if the alveolar thickness-to-radius ratio is greater than 0.05. Our model thus identifies the constraints on alveolar geometry and collagen waviness required for inflation stability and provides a multiscale link between alveolar pressure and stresses on fibres in healthy and diseased lungs.

1. Introduction

Mechanical stability of structures is critical for effective function and is usually associated with problems in physics and engineering. When a physical system is driven by external forces to the point of instability, it can suddenly transition from one configuration to a very different one. This often occurs in a catastrophic manner, such as when a bridge collapses. Mechanical stability is also critical in many biological systems that are subjected to significant stresses due to internal pressures. Inflation instability occurs in elastic balloons when the effective bulk modulus (the product of stiffness and volume) decreases monotonically with increasing volume. This eventually leads to a runaway phenomenon characterized by a negative bulk modulus. Inflation instability was discovered by Osborne at the beginning of the twentieth century [1] in rubber balloons. Surprisingly, however, Osborne also found that such instability does not exist in biology; when he inflated a urinary bladder, the transmural pressure P increased nearly exponentially with inflating volume V over the entire volume range. Indeed, detailed mathematical analysis suggests that a strong exponential-type nonlinearity in the stress–strain behaviour of the balloon wall is required to avoid inflation instability [2].

Although many studies have proposed that the mechanisms responsible for an exponential-type nonlinearity are the gradual collagen fibre realignment [3–6] and the sequential straightening of initially flaccid collagen fibrils [4,7], how these processes contribute to functional stability is not fully understood. In the lung, such a collagen recruitment process progressively takes over the load-bearing role from the much less stiff elastic fibres that bear most of the stress at low volumes [8,9]. However, neither the waviness distribution nor the rate at which collagen becomes recruited with increasing volume are known. Furthermore, the role of alveolar wall thickness and its thinning during large deformations associated with lung inflation has not been investigated. To this end, we report the development of a thick-walled sphere model containing linearly elastic elastin fibres and wavy but linearly elastic collagen fibres embedded in the extracellular matrix (ECM) of the wall. We provide an analytic solution for the pressure–volume behaviour of this model during large deformations as a function of the distribution of collagen waviness and the elastic stiffnesses of elastin and collagen. In addition, we report experimental data on collagen waviness in the alveoli, which allows us to estimate fibre stiffnesses and stresses. The combined contributions of the single wavy fibres and the thick-walled structure manifest in attaining the requirements for inflation stability in hollow biological structures that must bear internal pressure.

2. Results

2.1. Model development

The final equations are summarized below, while the details can be found in the Methods. The model considers a spherical, thick-walled alveolus (figure 1*a*). During isotropic expansion, an arbitrary radius R between the inner and outer radii ($R_i \le R \le R_e$) from the initial undeformed state stretches to a radius r between the deformed inner and outer radii ($r_i \le r \le r_e$) (figure 1*b*). Wavy collagen fibres and non-wavy elastin fibres are embedded within the matrix of the alveolar wall (figure 1*c*). In the undeformed state, no stress exists at the level of either the elastin or collagen fibres, and thus there is no stress in the alveolar wall. At the onset of expansion due to an alveolar pressure (P_{alv}) relative to the pressure outside the sphere, the elastin fibres immediately elongate and contribute to stress, while the collagen fibres initially become less wavy. Only when a collagen fibre is fully straightened, does it contribute to the circumferential stress $\sigma_{\theta\theta}$ (figure 1*e*). Radial stress σ_{rr} also builds up within the wall and is equal to P_{alv} at the inner radius.

Let Y_c and Y_e represent the elastic modulus of collagen and elastin, respectively. Defining a total fibre area fraction as the product of fibre number and average fibre cross-sectional area divided by the alveolar wall cross-sectional area, $\delta_{A,c}$ and $\delta_{A,e}$ are the total area fractions for collagen and elastin, respectively. We also define the effective fibre elastic modulus as $Y_{ce} = Y_c\,\delta_{A,c}$ and $Y_{ee} = Y_e\,\delta_{A,e}$ for collagen and elastin, respectively.

Collagen fibre waviness (w) is defined as the fibre contour length divided by its end-to-end distance in the undeformed state (figure 1*d*). Collagen fibre minimum and maximum waviness (i.e. when $P_{alv} = 0$) are denoted by w_1 and w_2, respectively. We assume that the waviness within a

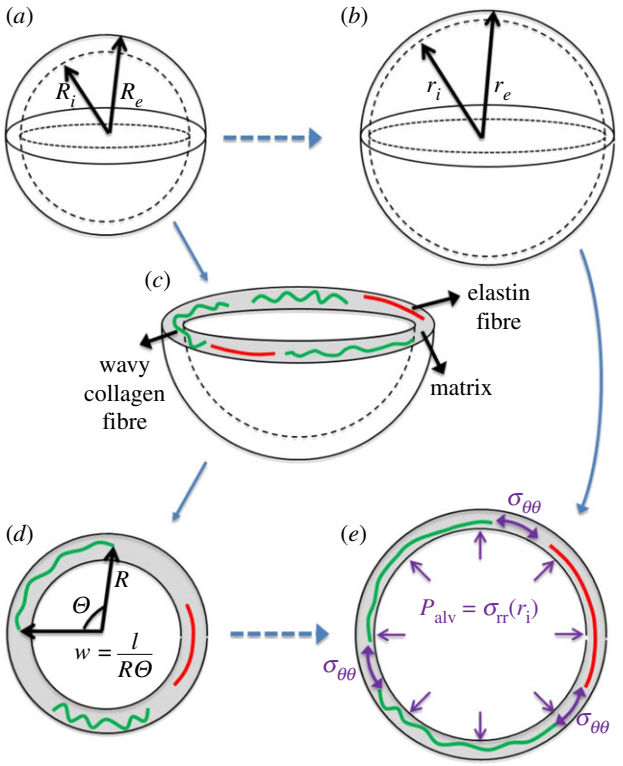

Figure 1. Alveolar model description. (*a*) A thick-walled spherical alveolus of initial inner and outer radii R_i and R_e, respectively. (*b*) As the alveolus expands isotropically, the wall thickness decreases as the stretched inner and outer radii r_i and r_e, respectively, increase. (*c*) Wavy collagen fibres (green) and the non-wavy elastin fibres (red) embedded in a matrix (grey) lie circumferentially within a plane slicing through the great circle of the sphere. (*d*) The waviness of a collagen fibre is defined as its contour length (l) over its end-to-end distance in the undeformed sphere. (*e*) As the alveolus expands due to alveolar pressure (P_{alv}), the wavy fibres become less wavy and, once fully straightened, they contribute together with the already elongated elastin fibres to the circumferential stress ($\sigma_{\theta\theta}$). Note that P_{alv} is equal to the radial pressure (σ_{rr}) at r_i.

population of fibres can be described by the beta probability distribution function (p) with two shape parameters α and β:

$$p(w) = \frac{(w - w_1)^{\alpha-1}(w_2 - w)^{\beta-1}}{B(\alpha,\beta)(w_2 - w_1)^{\alpha+\beta-1}}, \tag{2.1}$$

where $B(\alpha, \beta)$ is the β function of two variables (α and β).

Next, we introduce the circumferential stretch ratio $\lambda = r/R$, the inner stretch ratio $\lambda_i = r_i/R_i$ and a thickness mapping parameter $S = R/R_i$ that spans the distance through the septal wall thickness such that $1 \le S \le R_e/R_i = S_e$.

Based on this description, accounting for mass conservation, and using the deformed area in calculating stress, the Cauchy circumferential stress in the alveolar wall, at any given layer, due to elastin is

$$\sigma_{e,\theta\theta}(\lambda,S) = Y_{ee}\frac{\lambda}{S}(\lambda - 1), \tag{2.2}$$

whereas that due to the wavy collagen fibres is

$$\sigma_{c,\theta\theta}(\lambda,S) = \frac{Y_{ce}}{B(\alpha,\beta)\alpha(\alpha+1)}\frac{\lambda}{S}\frac{(\lambda - w_1)}{w_1}\left(\frac{\lambda - w_1}{w_2 - w_1}\right)^{\alpha} ((\alpha+1)A_1 - \alpha B_1), \quad w_1 \le \lambda < w_2 \tag{2.3}$$

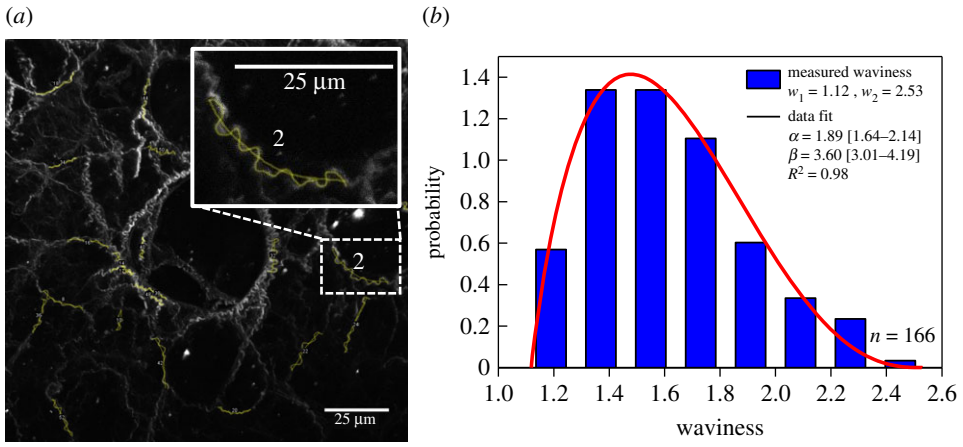

Figure 2. Collagen waviness results. (*a*) An SHG example image together with fibre tracings. Yellow traced lines are drawn over the fibre length and arc length. The former is divided by the latter to obtain the waviness of a single collagen fibre. The inset shows an enlarged section of a selected fibre. (*b*) Histogram and fit for all 166 measured fibres. Blue bar graph represents the experimental collagen waviness, while the red line is the fit of the beta distribution (equation (2.1)). The adjusted coefficient of determination R^2 is 0.98, and α and β values are 1.89 and 3.60, respectively (their 95% confidence intervals are shown in brackets). The minimum and maximum experimentally measured waviness values were 1.12 and 2.53, respectively.

and

$$\sigma_{c,\theta\theta}(\lambda, S) = \frac{Y_{ce}}{B(\alpha,\beta)\alpha(\alpha+1)}\frac{\lambda}{S}\frac{(\lambda - w_1)}{w_1} ((\alpha+1)A_2 - \alpha B_2), \quad \lambda \geq w_2, \tag{2.4}$$

where A_1, B_1, A_2 and B_2 are calculated from the Appell hypergeometric function of two variables (α and β) (see Model description in Methods)

The total circumferential stress ($\sigma_{\theta\theta}$) is then the summation of the individual fibre stresses ($\sigma_{\theta\theta}(\lambda, S) = \sigma_{e,\theta\theta} + \sigma_{c,\theta\theta}$). Since there are no shear stresses within the alveolar wall (see Methods), and applying the equations of equilibrium, the alveolar pressure due to the collagen and elastin fibres ($P_{\mathrm{alv},f}$) can be written as

$$P_{\mathrm{alv},f} = \frac{2}{\lambda_i^2}\int_1^{S_e} \frac{S^2}{(S^3 + \lambda_i^3 - 1)^{1/3}}\sigma_{\theta\theta}(\lambda, S)\, \mathrm{d}S. \tag{2.5}$$

Finally, assuming a thin-walled alveolus with initial thickness T_i, the stress across the wall is independent of r and equal to the mean stress ($\bar{\sigma}_{\theta\theta}$) evaluated at the middle layer which reduces equation (2.5) to the final analytical expression

$$P_{\mathrm{alv},f}(\lambda_i) \cong \bar{\sigma}_{\theta\theta}\left[\frac{(\lambda_i^3 + S_e^3 - 1)^{2/3}}{\lambda_i^2} - 1\right] \cong \bar{\sigma}_{\theta\theta}\left[\frac{(\lambda_i^3 + 3(T_i/R_i) + 3(T_i/R_i)^2 + (T_i/R_i)^3)^{2/3}}{\lambda_i^2} - 1\right]. \tag{2.6}$$

The corresponding alveolar air volume (V_{alv}) with an initial value of V_o is expressed as

$$V_{\mathrm{alv}} = V_o\lambda_i^3. \tag{2.7}$$

The total alveolar pressure (P_{alv}) also has a contribution due to surface tension γ [10] given by

$$P_{\mathrm{alv},s} = 2\frac{\gamma(r_i)}{r_i} = \frac{2\gamma(\Delta V/V_o)}{R_i(\Delta V/V_o + 1)^{1/3}}, \tag{2.8}$$

where $\Delta V = V_{\mathrm{alv}} - V_o$. We estimated γ as a function of ΔV by fitting a sigmoidal curve with three parameters to data collected by Smith & Stamenović [11], which resulted in the following relation (see electronic supplementary material for details):

$$\gamma\left(\frac{\Delta V}{V_o}\right) = \frac{33}{1 + \exp(-(\Delta V/V_o - 3)/0.5)}. \tag{2.9}$$

Finally, P_{alv} is the sum of $P_{\mathrm{alv},f}$ (equation (2.6)) and $P_{\mathrm{alv},s}$ (equation (2.8)). Thus, the final model includes eight parameters, six related to the fibres (Y_{ce}, Y_{ee}, α, β, w_1, w_2) and two related to alveolar geometry (S_e and V_o). For a known alveolar geometry, the model has only six parameters—the effective elastic modulus for elastin (Y_{ee}) and collagen (Y_{ce}), the minimum and maximum waviness of collagen (w_1 and w_2, respectively) and the two beta distribution shape parameters (α and β). The full derivation of equations (2.1)–(2.9), which also includes equations for engineering stress, stress for uniform fibre distribution, alveolar elastance, tension and collagen fibre stress distribution, is given in the Methods.

2.2. Collagen waviness

Before the model can be used to simulate or model *P–V* curves, parameters of the waviness distribution need to be determined. Figure 2 shows an example of our second-harmonic generation (SHG) image obtained in bovine lung tissue, and the corresponding probability distribution function for the collagen waviness. The distribution is skewed to the right and shows a wide range of waviness values from 1.12 to 2.53. The beta distribution fits the data well ($R^2 = 0.98$) with parameters $\alpha = 1.89$ and $\beta = 3.60$.

2.3. Model fitting

The model was able to provide good fits to human *P–V* curves (figure 3) taken from the literature [12–14]. Table 1 summarizes the population mean values of the estimated parameters both with and without the contribution from surface tension. The Akaike criterion suggests that including surface tension in the model does not improve the fit. Hence, for further analysis, we fit the model without surface tension.

2.4. Sensitivity analysis

To better understand how the model behaves, the effects of varying several parameters on the *P–V* curve are examined

Table 1. Human *P–V* curve fitting results. R^2, adjusted coefficient of determination; AICc, Akaike criterion; s.d., standard deviation. Numbers in brackets are the 95% confidence intervals.

	three-parameter fit without surface tension				
subject	R^2	Y_{ce} (kPa)	Y_{ee} (kPa)	w_1	AICc
Clements *et al.* 1961 [13]	0.987	1645 [945–2344]	14.2 [11.8–16.7]	1.31 [1.28–1.35]	69
Niewoehner *et al.* [14]	0.977	1262 [309–2214]	17.9 [8.6–27.1]	1.28 [1.19–1.37]	59
Verbeken *et al.* [12]	0.997	1352 [475–2228]	24.7 [16.1–33.4]	1.26 [1.18–1.34]	43
	mean ± s.d.	1419 ± 164	18.9 ± 4.3	1.28 ± 0.02	
	three-parameter fit with surface tension				
subject	R^2	Y_{ce} (kPa)	Y_{ee} (kPa)	w_1	AICc
Clements *et al.* [13]	0.988	1530 [755–2305]	13.7 [11.4–15.9]	1.32 [1.28–1.37]	81
Niewoehner *et al.* [14]	0.977	1071 [96–2046]	17.3 [8.1–26.5]	1.28 [1.17–1.39]	89
Verbeken *et al.* [12]	0.993	1139 [325–1954]	24 [15.6–32.4]	1.26 [1.17–1.34]	126
	mean ± s.d.	1247 ± 202	18.3 ± 4.3	1.29 ± 0.03	

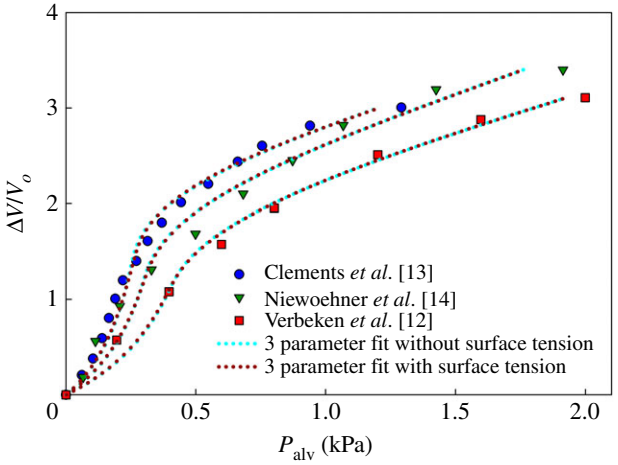

Figure 3. Results of fitting the three-parameter model. Fixing α, β and the range of collagen waviness ($w_2 - w_1$) using the experimental waviness measurements, three human isolated lung deflation *P–V* curves were fitted and Y_{ce}, Y_{ee} and w_1 were estimated (table 1). The fits with and without surface tension are almost indistinguishable.

in figure 4. Halving or doubling Y_{ee} shifted the curve to the left or right, respectively, though it had little effect on the *P–V* curve at higher P_{alv} (figure 4*a*). On the other hand, Y_{ce} affected $\Delta V/V_o$ at high P_{alv}: once collagen fibres became recruited, decreasing or increasing Y_{ce} halved or doubled the slope, respectively (figure 4*b*). Decreasing or increasing w_1 while keeping the width of the waviness distribution (dw) constant caused collagen fibres to become recruited earlier or later, respectively, allowing less or more volume expansion before reaching the upper inflection point (figure 4*c*), but there was little change in slope. Varying dw by fixing w_1 but decreasing or increasing w_2 did not affect the beginning location of the upper inflection point but increased or decreased, respectively, the final slope (figure 4*d*). Changing the waviness distribution towards a left-skewed distribution had a similar effect of increasing the slope (figure 4*e*). Finally, decreasing or increasing S_e had a similar effect as Y_{ee} by mainly shifting the curve, but these effects were still apparent at high P_{alv} (figure 4*f*). Note that in these simulations, pressure was used as input and $\Delta V/V_o$ as the output.

2.5. Alveolar inflation instability

An interesting feature of the *P–V* curve can be obtained by simulating equation (2.5) (and equations (2.3) and (2.4)) using volume as the input reaching values higher than those used in figure 3. For the baseline parameters (table 1), the *P–V* curve in figure 5 exhibits inflation instability in which P_{alv} increases to a maximum value, then decreases when $\Delta V/V_o$ further increases (figure 5*a*). The instability, however, occurs at non-physiologically high values of $\Delta V/V_o$. Expressed in terms of the effective bulk modulus (or specific alveolar elastance), $E_s = V_0 dP_{alv}/dV_{alv}$ (figure 5*b*), computed from equation (5.69), inflation instability can be partitioned into two regimes, geometric instability (decreasing but positive bulk modulus) starting at $\Delta V/V_0 = 7.3$ and $P_{alv} = 5.5$ kPa, and a runaway region (negative bulk modulus) beginning at $\Delta V/V_0 = 43.8$ and $P_{alv} = 10.4$ kPa, respectively (figure 5*d*, inset). Reductions in Y_{ce} and S_e, the absence of collagen, and changes in the waviness range and beta distribution parameters (both of which slowed collagen recruitment) resulted in inflation instability at much lower pressures compared to baseline (figure 5*c*,*d*). These lower pressures (figure 5*d*, inset) impinge on the physiological range (approx. 3 kPa for reduction in Y_{ce} and S_e).

2.6. Multiscale analysis

Beyond inflation instability, our model can be used to obtain new insight into alveolar wall mechanics. For example, figure 6 reveals the contribution of the fibres to the circumferential and radial stress and stiffness developed in the alveolar wall with increasing inner stretch ratio λ_i. Even though elastin is modelled as a linear material, it has a slightly nonlinear contribution to circumferential stress and stiffness (figure 6*a*,*d*, respectively). This is due to both geometric effects (wall thinning) in the model that are not enough to produce a convex shaped radial stress curve (figure 6*g*) as well as to stiffening behaviour (figure 6*j*). On the other hand, the nonlinear contribution to circumferential stress and stiffness by collagen (figure 6*b*,*e*,

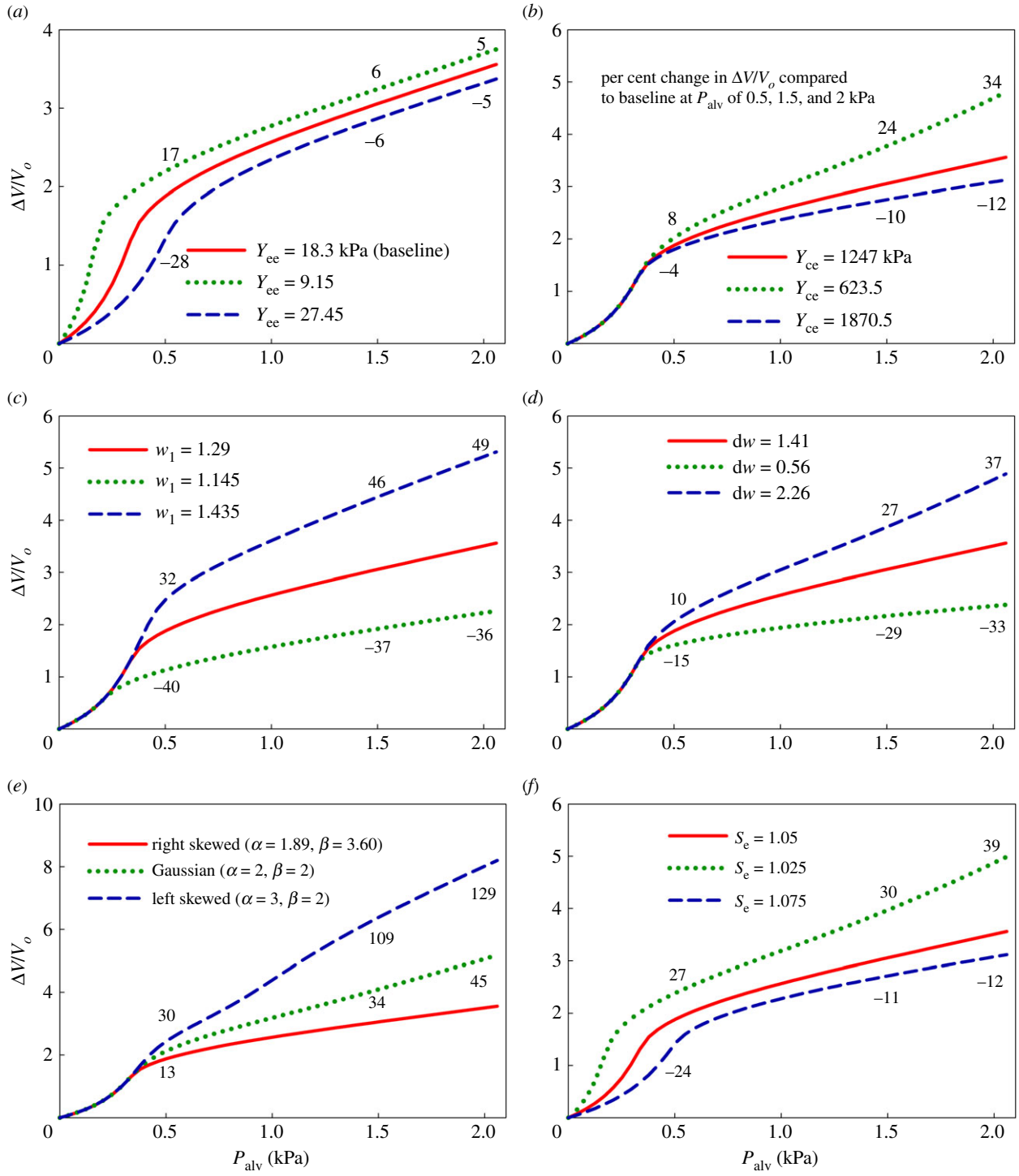

Figure 4. Sensitivity analysis. The plots show how the *P–V* curve is affected by variations in (*a*) waviness across the alveolar wall, (*b*) outer to inner radius ratio (S_e), (*c*) elastin effective elastic modulus, (*d*) collagen effective elastic modulus, (*e*) waviness range and (*f*) waviness distribution beta shape parameters (α and β). Per cent differences in $\Delta V/V_o$ from the baseline simulation are indicated next to each curve for P_{alv} of 0.5, 1.5 and 2 kPa.

respectively) is due both to fibre recruitment and wall thinning. In this case, we observe a convex radial stress–stretch ratio curve due mainly to collagen recruitment, which also leads to an increasing radial stiffness (figure 6*k*). The opposite contributions of elastin and collagen to the total alveolar stress and stiffness result in an initial geometric instability (but not inflation instability because it is not followed by runaway) followed by a strain-stiffening behaviour as collagen fibre recruitment contributes increasingly to alveolar stress (figure 6*c*,*i*) and stiffness (figure 6*f*,*l*).

While the collective elastin contribution to the alveolar wall stress is nonlinear, individual elastin fibres across layers experience linear stretch (figure 7*a*) and hence stress (figure 7*b*) with increasing λ_i. The variation across the wall is attributed to the different stretch ratios (λ) within the wall. Due to its waviness, collagen recruitment (figure 7*c*) leads to different stress distributions at a given λ_i as exemplified in figure 7*d*.

An interesting prediction of the model is the multiscale nature of stress spanning nearly six orders of magnitude (figure 8). At large inflation pressures, the alveolar wall circumferential stress is almost an order of magnitude greater than the alveolar pressure (radial stress at the inner wall). The stress on elastin fibres is nearly two orders of magnitude greater than the circumferential wall stress. The maximum stress carried by the collagen fibres is approximately two orders of magnitude greater than the elastin fibres.

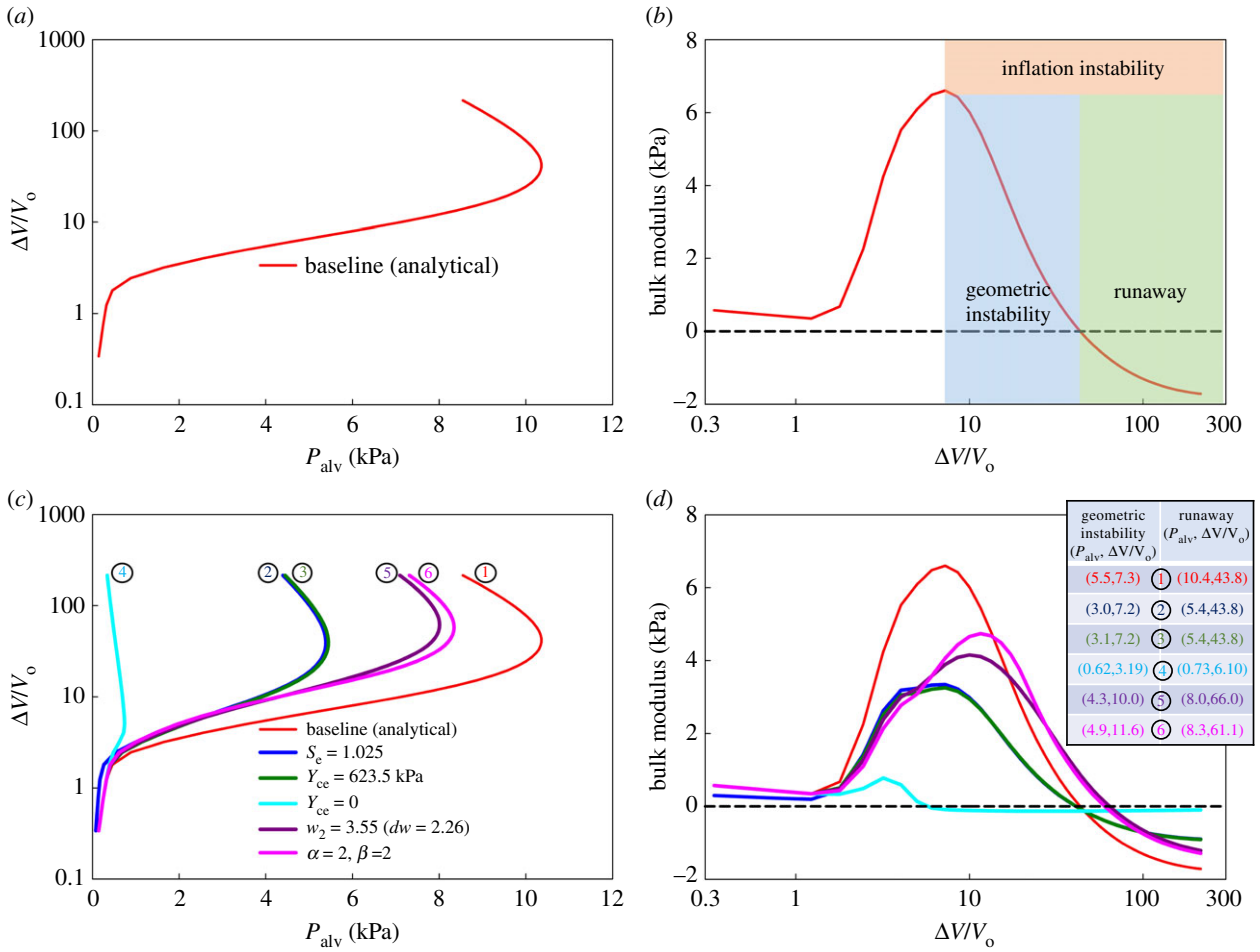

Figure 5. Inflation instability based on Cauchy stress (red solid line), reduced S_e (green), reduced Y_{ce} (green), absence of collagen (cyan), Gaussian distribution with the same waviness range (purple) and beta distribution with altered shape parameters (pink). (*a*) The *P–V* curve displays inflation instability at $\Delta V/V_o$. (*b*) Based on the incremental bulk modulus, inflation instability can be separated into a geometric instability regime (blue shaded region) and a runaway regime (green shaded region). (*c*) Compared to the baseline, all other simulations display inflation instability at lower pressures and (*d*) lower bulk modulus values. Note that $\Delta V/V_o$ was used as input to these simulations. *dw*, width of the waviness distribution.

3. Discussion

In this study, we developed an analytic thick-walled model of a single alveolus containing elastin and wavy collagen fibres embedded in tissue matrix undergoing large deformations. Based on a collagen waviness distribution obtained from SHG imaging, fitting the model to three human *P–V* curves allowed us to estimate the effective elastic moduli of the collagen and elastin components of alveolar tissue. We first verified the analytic results by showing that, given the known thickness to radius ratio of the alveolar walls, stress variation within the wall can be neglected (see electronic supplementary material, figure S2).

Our model also provides new insight into the roles that fibres and their recruitment play in determining bulk alveolar mechanics, and in particular how they ensure inflation stability to protect the alveolus from overdistension. In contrast with the traditional view that attributes alveolar inflation stability to the nonlinear stiffness behaviour of collagen fibres [15–17], we have demonstrated that stability can be achieved through linearly elastic but wavy collagen fibres that become progressively recruited into the load-bearing role as the alveolus inflates according to a waviness distribution that we observed experimentally (figure 2). The finite thickness of the alveolar wall is an important feature of our model because we show that inflation stability can be compromised by a decrease in the wall thickness-to-radius ratio as well as by a decrease in collagen fibre stiffness. These findings imply biological effects because alveolar strains can significantly influence the behaviour of cells embedded alveolar septa [18,19], with possible implications for drug treatments and mechanical ventilation strategies.

3.1. Collagen waviness

Measurements of waviness and curvature distributions [20] have been reported for some fibrils in lung parenchyma [21], including in vascular tissues [22]. However, to our knowledge, there has not been any previous assessment of collagen waviness distributions specifically within the alveolar wall. The most commonly evaluated fibril measurement is the so-called straightness parameter, defined as the end-to-end fibre distance over the contour length. Note that straightness is not exactly the reciprocal of our waviness definition since we used the arc length along the curved alveolar wall rather than the end-to-end distance. Rezakhaniha *et al*. [22] reported that the straightness parameter has a wide and left-skewed beta distribution ($\alpha = 4.47$, $\beta = 1.76$) with waviness exceeding 5. Our right-skewed beta distribution for waviness, with the lower range of 1.12–2.53, can be shown to be consistent with the straightness values of Rezakhaniha *et al*. [22].

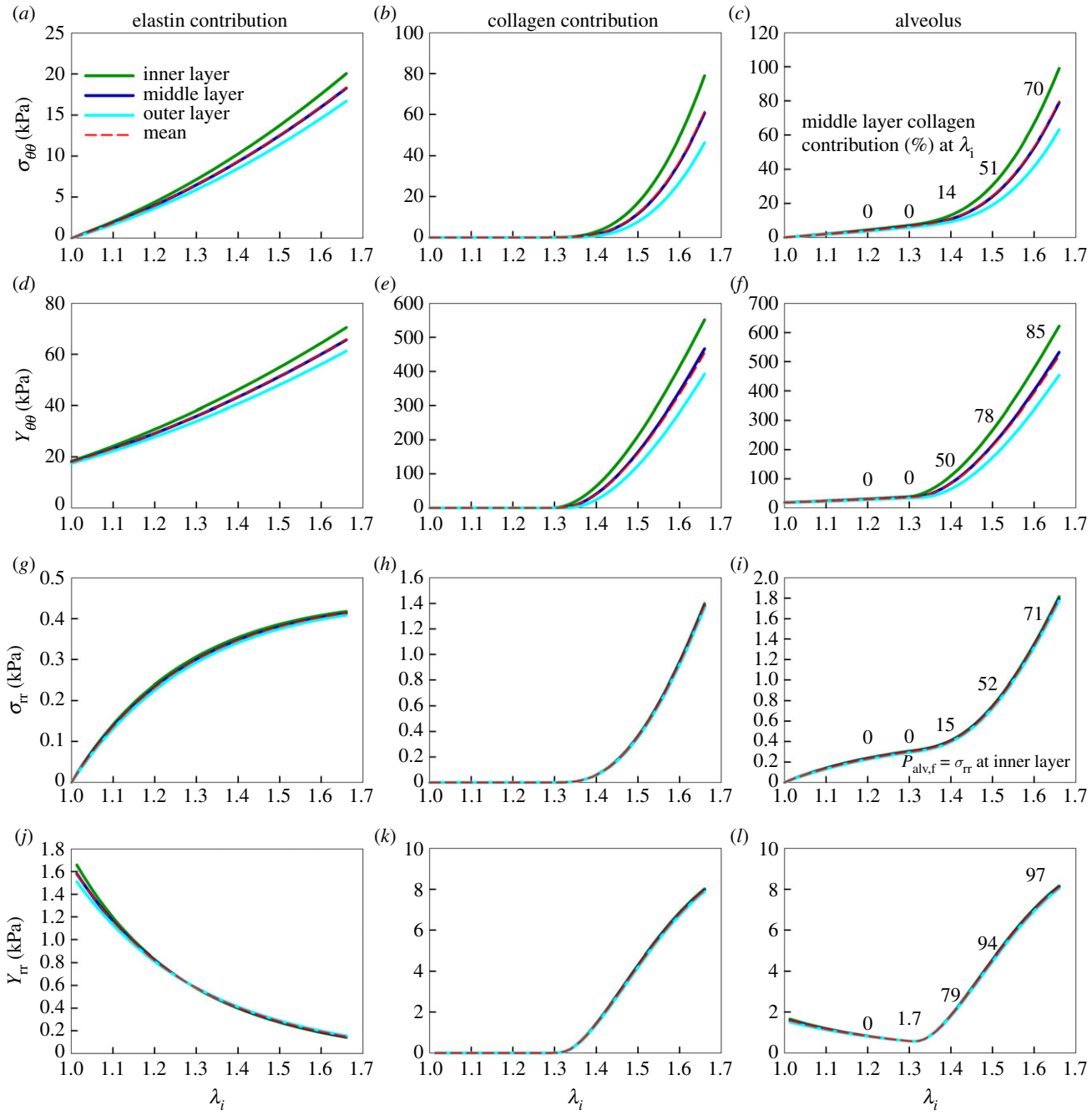

Figure 6. Alveolar wall stresses (σ) and stiffnesses (Y) due to the fibres as a function of the inner stretch ratio λ_i. Columns represent the contribution of elastin (column 1), collagen (column 2) and their combined effect (column 3) for the circumferential wall stress (row 1), circumferential wall stiffness (row 2), radial wall stress (row 3) and radial wall stiffness (row 4) for three different layers (solid lines) and the mean (red short-dashed line). Per cent contributions of collagen to the total stress and stiffness are shown in the third column at specific λ_i values (1.2, 1.3, 1.4, 1.5, 1.6). Note that the percentage contribution is the same for both circumferential and radial stresses. The alveolar pressure is equal to the radial stress evaluated at the inner layer. The nonlinear relationship between λ_i and alveolar pressure can be observed in (*i*). Individual layer circumferential stresses and stiffnesses were calculated analytically, while all other stress and stiffness values were obtained numerically.

The shape of the waviness distribution (figure 2) suggests that collagen fibres are initially recruited rapidly as the alveolus inflates, but the rate decreases as inflation continues. This is somewhat consistent with the general role of collagen fibre recruitment, together with their low extensibility [9,23]. However, our results also imply that collagen recruitment starts at a low circumferential strain of 0.29 corresponding to $\Delta V/V_o$ of 1.15 and P_{alv} of 0.3 kPa (figures 4*b* and 6*i*), as has been documented [24]. The estimated collagen waviness range (1.29–2.7) causes the initially recruited fibres to be stretched by 41% at the point where all fibres have been recruited. This is roughly double what is reported to be the maximum strain for stiff collagen fibres [23]. Nevertheless, within the range of fitted data (up to 1.96 kPa), not all fibres are recruited, and the maximum extension of those recruited is 29%, which is closer to the reported value of 20% [23]. On the other hand, elastin fibres are extended by approximately 170% of their initial lengths, which is close to their elastic limit [23].

3.2. Parameters from fitting

The elastic modulus of collagen has been found to be approximately100 MPa [25,26], while elastin fibres have an

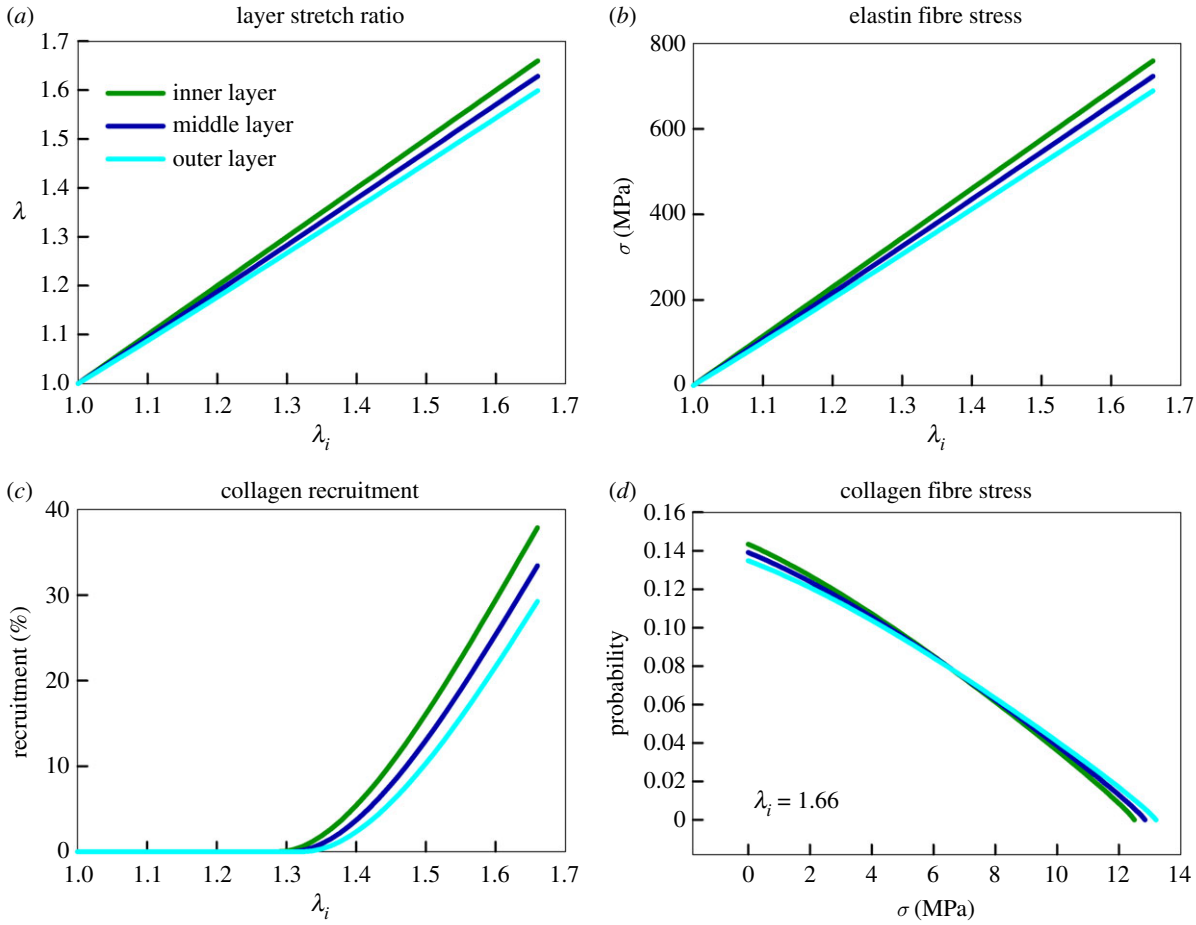

Figure 7. Single fibre analysis. (*a*) Due to the spherical geometry, the circumferential strain varies across alveolar wall layers, resulting in linearly varying stretch ratios within each of the three layers (inner, middle and outer layer). (*b*) Elastin fibre stress as a function of λ_i. (*c*) Collagen recruitment as a function of λ_i. (*d*) Collagen stress distribution at $\lambda_i = 1.66$.

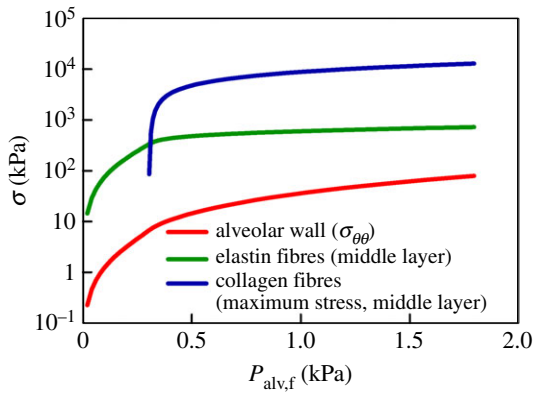

Figure 8. Multiscale stresses. The alveolar wall, elastin fibre and collagen fibre stresses can be related to $P_{alv,f}$, the alveolar pressure due to both collagen and elastin fibres. The total circumferential stress in the alveolar wall due to the fibres is shown by the red line. The collective elastin and collagen circumferential stresses in the middle layer are shown in green and blue, respectively. Note that the stress for collagen represents the maximum stress in the middle layer.

elastic moduli between 0.5 and 1 MPa [23,27,28]. Mercer & Crapo [21] reported that volume fractions of collagen and elastin in the human lung far from the alveolar duct are about 0.08 and 0.05, respectively. Published images show fibres running almost parallel to the alveolar wall, and thus are of comparable length [21]. The area fraction can then be estimated as being equal to the volume fraction. Using the area fractions deduced from Mercer & Crapo [21], the effective elastic moduli (elastic modulus times area fraction) of collagen and elastin are of the order of 10^3 and 10 kPa, respectively, which are comparable to our model-based estimates (table 1). Additionally, our model-based septal wall stiffness predictions are also consistent with recent direct AFM-based measurements [29].

3.3. Alveolar inflation stability and collagen waviness

The role of surfactant in lung deflation instability has been extensively studied [30,31]. However, surfactant does not play a major role in alveolar mechanics at higher lung volumes compared to collagen fibres [32,33]. Nevertheless, changes in surface forces and fibre mechanics together during inflation can lead to inflation instability when surface area and volume increase faster than pressure [34,35]. Both deflation and inflation instability of this kind are readily apparent from the Laplace Law

$$P_{alv} = \frac{2(T_f + \gamma)}{r_i}, \tag{3.1}$$

where T_f and γ are the tension due to the fibres and surface tension at the air–liquid interface, respectively. As the alveolus deflates, surfactant reduces γ at a faster rate than r_i, which decreases P_{alv}; otherwise, the decreasing r_i would increase P_{alv} and result in smaller alveoli emptying into larger ones leading to full collapse. This is referred to as deflation instability. Conversely, r_i increases during inflation, which decreases P_{alv} so that further alveolar inflation becomes progressively easier, leading to an infinitely large volume and zero pressure

in the limit. However, experiments clearly show that alveolar volume at high pressures increases only very slightly with pressure [36]. As $\Delta V/V_0 \to 0$, surface tension is not zero and the corresponding pressure approaches a constant (approx. 1 Pa). Although the model does not include a term that would balance this pressure, the value is small and does not influence the fitting. Surface tension has been found to increase linearly with volume [37,38] as well as reach a saturated constant value [13,39]. From equation (3.1), we conclude that the surface tension contribution to P_{alv} is at most proportional to r_i^2, which is less than the increase in alveolar volume, suggesting that surface tension alone is not able to achieve inflation stability. The contribution of surface tension to P_{alv} is indeed small (see electronic supplementary material, figure S3). Therefore, T_f/r_i must increase with r_i faster than $\Delta V/V_o$. Since the latter is a function of r_i^3, we find that $T_f/r_i \sim r_i^n$, where $n > 3$. When we combine the stress equation from the collagen fibres during recruitment (equation (2.3)) with the equation for tension (see Methods), we find that the tension from the fibres varies with r_i (or $\lambda(\lambda_i, S)$) as $T_f \sim r_i^{3+\alpha}$:

$$T_{f,\theta\theta}(\lambda_i, S, R_i) = \frac{\delta_f Y_f R_i \lambda^2}{B(\alpha,\beta)\alpha(\alpha+1)} \frac{\lambda - w_1}{w_1} \left(\frac{\lambda - w_1}{w_2 - w_1}\right)^{\alpha} ((\alpha+1)A_1 - \alpha B_1), \; w_1 \le \lambda < w_2. \tag{3.2}$$

Since $\alpha > 1$, stability is ensured, which is why the P–V curve is concave. However, after full recruitment of fibres, this is no longer the case ($T_f \sim r_i^3$) (see Methods). This may explain why the experimental measurements showed waviness over an extended range, allowing it to act as multiple layers of safety nets in cases of excessive inflation and thus ensuring inflation stability. Interestingly, after full recruitment of collagen, runaway inflation is still delayed due to the combination of high collagen elastic modulus and appropriate S_e ratio. Mechanical failure (yielding) is eventually inevitable, but it will occur at very high (non-physiological) pressures (figure 5). Thus, stability requires a specific waviness distribution that allows continuous recruitment of collagen fibres over the physiological range of pressures.

The model predicts that the bulk modulus of the sphere becomes negative at a critical value of stretch ratio or relative volume change (figure 5). Negative moduli have been observed during lung inflation and interpreted as an emergent behaviour stemming from avalanche-like opening of many alveoli [40]. For a single sphere, a maximum in pressure during inflation is also called limit-point instability, which was first observed in rubber balloons by Osborne in 1909 [1]. Theoretical analysis showed that strain-hardening that is a characteristic property of biological materials can eliminate the instability [2]. While many previous studies have associated the strain-hardening behaviour with collagen alignment or recruitment, our study also shows that the specific distribution of waviness pushes the instability beyond the physiological range of pressures.

3.4. Physiological implications

Our study considers specific physiological entities (i.e. wavy fibres) in a test of the thin-walled assumption of the famous Laplace Law as a description of the alveolus (equation (3.1)). The consistency between the analytically calculated pressure using the middle layer and the numerically integrated mean across the thickness of the alveolar wall (electronic supplementary material, figure S2) suggests that a single layer of fibres of appropriate tensile strength can sustain the same pressures as multiple layers. This is important because the alveolar interstitium, which includes fibres as well as other components, takes up only 56% of all the alveolar wall [41], so not every structure across the wall maintains stress. Using a single layer also allows us to analytically relate stresses at different scales (figure 8). Nevertheless, a single layer may be fragile to mechanical failure of the alveolar wall, something that is central to oedema formation [42] and to emphysema progression [43]. Furthermore, while R_i is species dependent, S_e was estimated to be species independent (see electronic supplementary material for details). This may have implications for why larger alveoli are able to maintain inflation stability despite varying alveolar size. If S_e is maintained across species, then the pressure contributed by the fibres does not depend on alveolar geometry but on the fibre content and stiffness.

Our model analysis also allows the estimation of the separate contributions of structural (e.g. wall thickness and waviness) and constitutive properties (e.g. elastic modulus) to the P–V curve. It is currently not known whether parenchymal reorganization or abnormal fibre stiffness contributes more to the observed physiological phenotype of a given disease. Collagen content has been found to increase in the ageing lung [44], while an organizational change in the parenchyma has been shown to play a role in both fibrosis and emphysema [45,46]. Our model allows specific predictions of each effect on the P–V curve.

An interesting insight into lung physiology is related to the initial convexity (or increase in compliance) of the deflation P–V curve. Our simulations demonstrate that this occurs at the level of a single alveolus (e.g. figure 5*b* at $P < 1$ kPa) suggesting that this convexity can be explained by an inability of the linearly elastic elastin fibres alone to counteract inflation instability, and that it is only after collagen recruitment starts to occur that the P–V curve achieves its characteristic concavity at higher pressures. In fact, without collagen, the lung would be unstable at breathing pressures (cyan, figure 5*c*) and hence unable to support respiration. Additionally, our waviness imaging together with the modelling suggest that collagen recruitment starts relatively early during inflation, which is in contrast with the classical belief that collagen fibres only contribute at high pressures. This finding has also been proposed based on collagen digestion in lung tissue strips [47].

3.5. Model limitations

Our model is not without limitations. First, we do not consider species-dependent properties because such data are not available for waviness, and surface tension does not seem to vary between species [48]. Second, we assumed linearly elastic collagen fibres. To our knowledge, stress–strain curves from single fibres isolated from the lung have not been reported. However, a linear behaviour of isolated collagen fibrils has been reported [49,50]. Third, the model does not include network effects arising through alveolar interactions, and does not consider changes in volume that occur in the alveolar ducts and airways. Our basic assumption is that the relative change in volume is the same in every alveolus, which allows us to model the whole lung P–V curve using a single alveolus. The effects of surface tension, however, are correctly considered at the single alveolus scale. Although the alveolus may not be a perfect sphere and hence the Laplace Law would not apply for the surface tension [51–55], we found that surface tension is

less important along the deflation limb of the *P–V* curve and especially at high lung volumes. We also neglect fibre–fibre interactions, which could further contribute to alveolar mechanics, especially those involving energy dissipation [56]. However, from images of human lung parenchyma, Matsuda *et al*. [53] noted that collagen and elastin fibre bundles run parallel to each other within the alveolar mouth without intertwining, then they separate at different locations and run independently from one another within the septal walls. This suggests minimal interaction between the two fibre systems. The model also assumes affine transformation in that the stretch ratio within the wall thickness is transmitted to the fibres. If the deformation is not affine, the waviness range would be overestimated. Nevertheless, the role of waviness and the conclusions we have drawn would not change. In future work, imaging fibre waviness under stretch could resolve this question. Finally, modelling only a single alveolus ignores important force symmetries that exist in a three-dimensional alveolar network in which adjacent alveoli share a common septal wall; the outside of one wall is the inside of the other. This may impose limitations on the possible waviness distributions across the wall thickness. More importantly, interactions between alveoli in a network may influence inflation stability in ways that cannot be captured by considering a single alveolus in isolation [10,57]. In this study, we have focused on the stability of a single alveolus, which, to our knowledge, has not been examined in the light of the contribution of collagen waviness within the alveolar walls. We found that waviness acts as a safety net in cases of excessive inflation and thus ensures stability, which suggests that the contribution of collagen to alveolar stability may occur at lower lung volumes than previously thought due primarily to the wide distribution of waviness, which we treated analytically. Despite these limitations, the model offers novel insight into alveolar mechanics and inflation stability, and provides a framework for estimating ECM stresses and strains that are vital for mechanotransduction.

4. Conclusion

Modelling the behaviour of elastin and collagen fibres inside thick-walled alveoli under large deformation shows the importance of invoking conservation of mass for the accurate calculation of alveolar pressure, permits an understanding of the contributions of the two fibre types to the *P–V* curve and demonstrates the key role of collagen waviness in ensuring *P–V* inflation stability. Modelling also provides estimates of strains and stresses at the level of a single alveolus and single fibres. The accurate estimation of these stresses is crucial in a number of areas including studying the response of cells to mechanical cues, avoiding tissue damage in ventilator-induced lung injury and distinguishing structural from material changes in healthy and diseased lungs.

5. Methods

5.1. Model derivation

5.1.1. Model description

5.1.1.1. Alveolus

The model considers a thick-walled alveolus and assumes spherical geometry. The alveolar wall is described in terms of a spherical coordinate system with uppercase ($R_i \le R \le R_e$, $0 \le \Theta \le 2\pi$, $0 \le \Phi \le 2\pi$) and lowercase ($r_i \le r \le r_e$, $0 \le \theta \le 2\pi$, $0 \le \phi \le \pi$) symbols representing the undeformed and the deformed state, respectively. The inner and outer radii are denoted by R_i and R_e, which become r_i and r_e, respectively, during inflation. We define a general stretch ratio $\lambda = r/R$ for any radius within the thickness of the wall, an inner stretch ratio $\lambda_i = r_i/R_i$ and an outer stretch ratio $\lambda_e = r_e/R_e$. We also introduce a thickness mapping parameter $S = R/R_i$ to span across the alveolar thickness so that $S_i = 1 \le S \le R_e/R_i = S_e$. The wall is assumed to be incompressible, homogeneous isotropic and deforms such that angles are preserved during expansion ($\theta = \Theta$, $\phi = \Phi$). Consequently, alveolar expansion is isotropic and homogeneous, maintaining its spherical structure as it inflates.

5.1.1.2. Wavy fibres

The wall contains wavy fibres embedded in the ECM that are oriented in the circumferential direction. Each fibre forms a continuous loop around the wall. When the alveolus is inflated, the wavy fibres are gradually straightened; a fibre bears no load so long as it is wavy (flaccid), but as soon as it is stretched to the point of becoming straight, it begins to bear load upon further stretch. Fibres act as linear springs in parallel without any fibre–fibre or fibre–matrix interaction. Thus, nonlinearity in the mechanical behaviour of the system as a whole arises purely from the manner in which wavy fibres become recruited with stretch. None of the fibres is stretched at any radius R in the undeformed state. This guarantees that there is no residual stress across the wall before the alveolus becomes inflated above its baseline volume. If N_f is the total number of fibres in the alveolar wall with an average cross-sectional area A_f and average elastic modulus Y_f, the fraction of the cross-section occupied by fibres in the undeformed state of the wall is approximately $\delta_{A,f} = N_f A_f / 2\pi R_i (R_e - R_i)$ provided that the wall is thin. This assumption is supported by experimental studies suggesting that $R_e/R_i \approx 1.05$ [58–60] (see electronic supplementary material for details).

Next, we assume that wavy fibres are distributed across the thickness of the wall. For a given contour length, or unstretched length, of a fibre, denoted by L_f, we define a corresponding contour radius as $R_f = L_f/2\pi$. The waviness of a fibre at radius R is, therefore, $w_f(R) = L_f/2\pi R = R_f/R$. We also define w_1 and w_2 as the minimum and maximum waviness at S_e, respectively. The probability distribution of R_f, denoted by $p_f(R_f, R)$, can be a function of R and is defined as the probability of finding fibres with contour radius between R_f and $R_f + \mathrm{d}R_f$ within the alveolar wall between radii R and $R + \mathrm{d}R$, and between angles Θ and $\Theta + \mathrm{d}\Theta$, and between Φ and $\Phi + \mathrm{d}\Phi$ such that

$$\iint p_f(R_f, R)\, \mathrm{d}R_f\, \mathrm{d}R \mathrm{d}\Theta \mathrm{d}\Phi = 1. \tag{5.1}$$

Since fibre waviness is independent of angles, equation (5.1) can be simplified as

$$\int p_f(R_f, R)\, \mathrm{d}R_f\, \mathrm{d}R = 1. \tag{5.2}$$

In terms of the dimensionless parameters w_f and S, the probability distribution is written as

$$\iint p_{w_f}(w_f, S)\, \mathrm{d}w_f\, \mathrm{d}S = 1 \tag{5.3}$$

Since the range of waviness may vary across the wall, we take this into account by using a function $G_o(S)$ such that $w_1 G_o(S) \le w_f \le w_2 G_o(S)$. When $G_o = 1$, the waviness distribution becomes independent of S and hence uniform throughout the wall thickness. Alternatively, if we set $G_o(S) = (S_e + 1)/2S$ such that $w_1(S_e + 1)/2S \le w_f(S) \le w_2(S_e + 1)/2S$, the waviness of the fibres will decrease with S. $G_o = 1$ allows the fibres to have constant waviness but with linearly increasing fibre length across the alveolar wall, while $G_o(S) = (S_e + 1)/2S$ implies a decrease

in waviness but uniform fibre length across the wall. Note, however, that for this specific case, the waviness of the middle layer ($S = (S_e + 1)/2$) is the same for the two cases.

For a given S, we shall describe the waviness within the wall with the general beta distribution, which includes the beta function $B(\alpha, \beta)$ with its shape parameters α and β. By varying G_o, it is possible to shift the waviness range across S, while changing α and β allows different shapes for the waviness distribution. For instance, when $\alpha = \beta = 1$, the beta distribution, and hence p_{w_f}, becomes uniform. With these considerations, the general form of the waviness distribution is written as

$$p_{w_f}(w_f, S) = \frac{1}{S_e - 1} \frac{(w_f - w_1 G_o)^{\alpha-1}(w_2 G_o - w_f)^{\beta-1}}{B(\alpha,\beta)(w_2 G_o - w_1 G_o)^{\alpha+\beta-1}} \tag{5.4}$$

5.1.1.3. Matrix

If N_m is the total number of ECM units with average cross-sectional area and elastic modulus of A_m and Y_m, respectively, then the fractional area of the matrix is $\delta_{A,m} = N_m A_m / 2\pi R_i (R_e - R_i)$. We assume these units are distributed throughout the tissue according to a uniform distribution $p_m(R) = 1/R_e - R_i$.

5.1.1.4. Stresses and pressures

The following derivation is based on the model of Wuyts *et al*. [61] who developed a thick-walled cylindrical model of the aorta. However, using the beta distribution for fibre waviness, instead of the Lorentz function in their model, we can obtain analytic expressions for the true stress and the incremental stiffness across the thickness of an alveolus under large deformations.

5.1.2. Mass conservation

To derive the P–V curve, let us first consider a spherical shell with its inner radius R_i and thickness $\mathrm{d}R$, $0 \le \theta \le 2\pi$ and $0 \le \phi \le \pi$. By assuming incompressibility and applying the conservation of mass for a layer between R_i and $R = R_i + \mathrm{d}R$, we obtain the following relations

$$\frac{4}{3}\pi(R^3 - R_i^3) = \frac{4}{3}\pi(r^3 - r_i^3), \tag{5.5}$$

$$R = (r^3 - r_i^3 + R_i^3)^{1/3} \tag{5.6}$$

and

$$\frac{\mathrm{d}R}{\mathrm{d}r} = \frac{r^2}{(r^3 - r_i^3 + R_i^3)^{2/3}} = \frac{r^2}{R^2} = \lambda^2, \tag{5.7}$$

where λ is the stretch ratio. Note that equation (5.7) is the inverse of the deformation gradient in r. Solving equation (5.6) for r^3 and dividing with R_i^3, we can relate the general stretch ratio as a function of the internal stretch ratio (λ_i) to the thickness mapping parameter (S)

$$\lambda^3(\lambda_i, S) = \frac{S^3 + \lambda_i^3 - 1}{S^3}. \tag{5.8}$$

5.1.3. Wavy fibre circumferential stress

Let us now consider how the circumferential force at radius r arises in the deformed state. As a circumferential layer of tissue at R is stretched, a fibre with R_f is recruited when the layer is stretched to $r = R_f$. Further inflating the alveolus stretches the layer and the strain on the fibre is $(2\pi r - 2\pi R_f)/2\pi R_f$. The corresponding force ($f_{s,f}$) of the fibre acting perpendicular to a small surface area element $r\mathrm{d}\theta\mathrm{d}r$ in the deformed state is the fibre stress, given as the product of modulus, fibre strain and fibre area

$$f_{s,f} = \begin{cases} Y_f A_f \dfrac{r - R_f}{R_f} = Y_f A_f \left(\dfrac{\lambda - w_f}{w_f}\right) & r > R_f \text{ or } \lambda > w_f \\ 0 & \text{otherwise} \end{cases} \tag{5.9}$$

The total circumferential force due to all fibres (f_f) corresponding to a given waviness within a small layer of the wall is thus given by

$$\mathrm{d}(\mathrm{d}f_f) = N_f p_{w_f}(w_f, S) Y_f A_f \left(\frac{\lambda - w_f}{w_f}\right) \mathrm{d}w_f \, \mathrm{d}S. \tag{5.10}$$

The circumferential true stress in the wall is obtained by dividing this force with the deformed area, $2\pi r \mathrm{d}r = (2\pi R_i^2 S \mathrm{d}S/\lambda)$, derived from equations (5.6, 5.7 and 5.8). The Cauchy stress is written as

$$\mathrm{d}\sigma_{f,\theta\theta} = N_f p_{w_f}(w_f, S) Y_f A_f \left(\frac{\lambda - w_f}{w_f}\right) \frac{\lambda \mathrm{d}w_f \, \mathrm{d}S}{2\pi R_i^2 S \, \mathrm{d}S}. \tag{5.11}$$

If we divide the right-hand side of equation (5.11) with $(R_e - R_i)$ and multiply it by $R_i(S_e - 1) = R_e - R_i$, we can use the fibre area fraction to simplify equation (5.11) as follows:

$$\mathrm{d}\sigma_{f,\theta\theta} = \frac{N_f A_f}{2\pi(R_e - R_i)R_i} \, p_{w_f}(w_f, S) Y_f (S_e - 1) \frac{\lambda}{S} \left(\frac{\lambda - w_f}{w_f}\right) \mathrm{d}w_f \tag{5.12}$$

and

$$\mathrm{d}\sigma_{f,\theta\theta} = \delta_f \, Y_f p_{w_f}(w_f, S)(S_e - 1) \frac{\lambda}{S} \left(\frac{\lambda - w_f}{w_f}\right) \mathrm{d}w_f. \tag{5.13}$$

Replacing $p_{w_f}(w_f, S)$ with the beta distribution from equation (5.4) gives

$$\mathrm{d}\sigma_{f,\theta\theta} = \delta_f \, Y_f \frac{\lambda}{S} \frac{(w_f - w_1 G_o)^{\alpha-1}(w_2 G_o - w_f)^{\beta-1}}{B(\alpha,\beta)(w_2 G_o - w_1 G_o)^{\alpha+\beta-1}} \left(\frac{\lambda - w_f}{w_f}\right) \mathrm{d}w_f. \tag{5.14}$$

Finally, to simplify the integration, the following substitutions for w_f and λ are applied, respectively

$$w_t = \frac{w_f - w_1 G_o}{w_2 G_o - w_1 G_o} \tag{5.15}$$

and

$$\lambda_t = \frac{\lambda - w_1 G_o}{w_2 G_o - w_1 G_o}. \tag{5.16}$$

When fibres are being recruited the stretch ratio satisfies $w_1 G_o \le \lambda < w_2 G_o$, which is equivalent to $0 \le w_t < \lambda_t$ and $0 \le \lambda_t < 1$, whereas for fully recruited fibres, $\lambda \ge w_2 G_o$, which yields $0 \le w_t \le 1$ and $1 \le \lambda_t < \infty$. The probability distribution function for $p_f(w_t)$ is now written as:

$$p_f(w_t) = \frac{1}{(S_e - 1)} \frac{1}{B(\alpha, \beta)} (w_t)^{\alpha-1}(1 - w_t)^{\beta-1}, \tag{5.17}$$

where $0 \le w_t \le 1$ for any layer S as required by the beta distribution. Thus, the differential stress is given by

$$\mathrm{d}\sigma_{f,\theta\theta} = \delta_f \, Y_f \frac{\lambda_t(w_2 G_o - w_1 G_o) + w_1 G_o}{S} \frac{w_t^{\alpha-1}(1 - w_t)^{\beta-1}}{B(\alpha, \beta)} \left(\frac{\lambda_t - w_t}{w_t(w_2 G_o - w_1 G_o) + w_1 G_o}\right)(w_2 G_o - w_1 G_o) \, \mathrm{d}w_t. \tag{5.18}$$

Integrating equation (5.18) over the entire range of waviness gives the true circumferential stress due to all fibres at a given layer S experiencing a stretch ratio $\lambda(\lambda_i, S)$ as

$$\sigma_{f,\theta\theta}(\lambda_i, S) = \frac{\delta_f Y_f}{B(\alpha,\beta)\alpha(\alpha + 1)} \frac{\lambda}{S} \frac{\lambda - w_1 G_o}{w_1 G_o} \left(\frac{\lambda - w_1 G_o}{w_2 G_o - w_1 G_o}\right)^{\alpha} \qquad ((\alpha + 1)A_1 - \alpha B_1) \quad \text{for } w_1 G_o \le \lambda < w_2 G_o \tag{5.19}$$

and

$$\sigma_{f,\theta\theta}(\lambda_i,S) = \frac{\delta_f Y_f}{B(\alpha,\beta)\alpha(\alpha+1)}\frac{\lambda}{S}\frac{\lambda - w_1G_o}{w_1G_o}((\alpha+1)A_2 - \alpha B_2)\,, \quad \text{for } \lambda \geq w_2G_o \tag{5.20}$$

where

$$A_1 = F_1\left(\alpha; 1-\beta, 1\,; \alpha+1; \frac{\lambda - w_1G_o}{w_2G_o - w_1G_o}, -\frac{\lambda - w_1G_o}{w_1G_o}\right), \tag{5.21}$$

$$B_1 = F_1\left(\alpha+1; 1-\beta, 1\,; \alpha+2; \frac{\lambda - w_1G_o}{w_2G_o - w_1G_o}, -\frac{\lambda - w_1G_o}{w_1G_o}\right), \tag{5.22}$$

$$A_2 = F_1\left(\alpha; 1-\beta, 1\,; \alpha+1; 1, -\frac{w_2 - w_1}{w_1}\right) \tag{5.23}$$

and

$$B_2 = F_1\left(\alpha+1; 1-\beta, 1\,; \alpha+2; 1, -\frac{w_2 - w_1}{w_1}\right), \tag{5.24}$$

and F_1 is the Appell hypergeometric function of two variables defined as

$$F_1(a; b,b'; c; x,y) = \sum_{m=0}^{\infty}\sum_{n=0}^{\infty}\frac{a_{m+n}b_m b'_n}{m!n!c_{m+n}}x^m y^n, \tag{5.25}$$

which converges when $|x|<1$, $|y|<1$. Also, note that λ in these equations is a function of λ_i according to equation (5.8) and the stresses are zero for $\lambda \leq w_1G_0$.

5.1.4. Engineering stress

In most experimental cases, it is the engineering stress (σ_e) that is actually calculated. Hence, we can divide equation (5.10) by the undeformed area ($2\pi RdR$) rather than the deformed area ($2\pi rdr$). Interestingly, this results in a factor of λ, where $\sigma_e = \sigma/\lambda$, for the stress equation as a consequence of the conservation of mass (equation (5.5)).

5.1.5. Uniform distribution stress and stiffness

For the special case of a uniform distribution of waviness ($\alpha = \beta = 1$), p_f is written as

$$p_{w_f}(w_f,S) = \frac{1}{S_e - 1}\frac{1}{G_o}\frac{1}{w_2 - w_1}. \tag{5.26}$$

Following the same procedure as above, the true stress simplifies to:

$$\sigma_{f,\theta\theta}(\lambda_i,S) = \frac{\delta_f Y_f}{w_2 - w_1}\frac{1}{G_o}\frac{\lambda^2}{S}\left[ln\left(\frac{\lambda}{w_1G_o}\right) + \frac{w_1G_o}{\lambda} - 1\right], \quad \text{for } w_1G_o \leq \lambda < w_2G_o \tag{5.27}$$

and

$$\sigma_{f,\theta\theta}(\lambda_i,S) = \frac{\delta_f Y_f}{w_2 - w_1}\frac{1}{G_o}\frac{\lambda^2}{S}\left[\ln\left(\frac{w_2}{w_1}\right) + \frac{w_1G_o}{\lambda} - \frac{w_2G_o}{\lambda}\right], \quad \text{for } \lambda \geq w_2G_o. \tag{5.28}$$

Differentiating equations (5.27) and (5.28) with respect to λ provides the incremental Young's modulus (E_f) for the thick-walled sphere as

$$E_{f,\theta\theta}(\lambda_i,S) = \frac{\delta_f Y_f}{w_2 - w_1}\frac{1}{G_o}\frac{\lambda}{S}\left[2\ln\left(\frac{\lambda}{w_1G_o}\right) + \frac{w_1G_o}{\lambda} - 1\right], \quad \text{for } w_1G_o \leq \lambda < w_2G_o \tag{5.29}$$

and

$$E_{f,\theta\theta}(\lambda_i,S) = \frac{\delta_f Y_f}{w_2 - w_1}\frac{1}{G_o}\frac{\lambda}{S}\left[2\ln(w_1) + \frac{w_1G_o}{\lambda} - \frac{w_2G_o}{\lambda}\right], \quad \text{for } \lambda \geq w_2G_o \tag{5.30}$$

The engineering stress and incremental tissue stiffness (E_e) are then given by

$$\sigma_{e_{f,\theta\theta}}(\lambda_i,S) = \frac{\delta_f Y_f}{w_2 - w_1}\frac{1}{G_o}\frac{\lambda}{S}\left[\ln\left(\frac{\lambda}{w_1G_o}\right) + \frac{w_1G_o}{\lambda} - 1\right], \quad \text{for } w_1G_o \leq \lambda < w_2G_o, \tag{5.31}$$

$$\sigma_{e_{f,\theta\theta}}(\lambda_i,S) = \frac{\delta_f Y_f}{w_2 - w_1}\frac{1}{G_o}\frac{\lambda}{S}\left[\ln\left(\frac{w_2}{w_1}\right) + \frac{w_1G_o}{\lambda} - \frac{w_2G_o}{\lambda}\right], \quad \text{for } \lambda \geq w_2G_o, \tag{5.32}$$

$$E_{e_{f,\theta\theta}}(\lambda_i,S) = \frac{\delta_f Y_f}{w_2 - w_1}\frac{1}{G_o}\frac{1}{S}\ln\left(\frac{\lambda}{w_1G_o}\right), \quad \text{for } w_1G_o \leq \lambda < w_2G_o \tag{5.33}$$

and

$$E_{e_{f,\theta\theta}}(\lambda_i,S) = \frac{\delta_f Y_f}{w_2 - w_1}\frac{1}{G_o}\frac{1}{S}\ln\left(\frac{w_2}{w_1}\right), \quad \text{for } \lambda \geq w_2G_o. \tag{5.34}$$

5.1.6. Circumferential extracellular matrix stress

The circumferential force generated by the ECM can be derived similarly, but without considering waviness. Accordingly, the force is written as

$$\mathrm{d}(\mathrm{d}f_m) = N_m p_m(R) A_m Y_m \frac{r-R}{R}\mathrm{d}R. \tag{5.35}$$

Dividing by the deformed area $2\pi rdr$, the ECM true stress is given by

$$\sigma_{m,\theta\theta}(r,R(r)) = \frac{N_m A_m Y_m}{2\pi(R_e - R_i)}\frac{r-R}{R}\frac{\mathrm{d}R}{r\mathrm{d}r} = \frac{N_m A_m Y_m}{2\pi(R_e - R_i)}\left(\frac{r^2 - rR}{R^3}\right). \tag{5.36}$$

Multiplying the numerator and denominator by R_i and writing the equation as a function of $\lambda(\lambda_i, S)$ and S gives

$$\sigma_{m,\theta\theta}(\lambda_i, S) = \delta_m Y_m \frac{\lambda}{S}(\lambda - 1). \tag{5.37}$$

Differentiating equation (5.37) with respect to λ provides the incremental Young's modulus of the matrix

$$E_{m,\theta\theta}(\lambda_i, S) = \delta_m Y_m \frac{1}{S}[2\lambda - 1], \tag{5.38}$$

while the engineering stress and stiffness are equal to

$$\sigma_{e_{m,\theta\theta}}(\lambda_i, S) = \delta_m Y_m \frac{1}{S}(\lambda - 1) \tag{5.39}$$

and

$$E_{e_{m,\theta\theta}}(\lambda_i, S) = \delta_m Y_m \frac{1}{S}. \tag{5.40}$$

5.1.7. Total circumferential stress

The total circumferential true stress $\sigma_{\theta\theta}$ and the corresponding stiffness $E_{\theta\theta}$ of the tissue arise from the summed combination of both the fibres and the matrix ($\sigma_{\theta\theta} = \sigma_{f,\theta\theta} + \sigma_{m,\theta\theta}$, $E_{\theta\theta} = E_{f,\theta\theta} + E_{m,\theta\theta}$). Furthermore, the fibre equation can be split into two or more entities (i.e. collagen and elastin) to account for fibres with different material and waviness properties.

Finally, the average circumferential stress across the wall at a given λ_i can be calculated as

$$\bar{\sigma}_{\theta\theta}(\lambda_i) = \frac{\int_{S_o}^{S_1} \sigma_{\theta\theta}(\lambda(\lambda_i,S),S)\mathrm{d}S \; + \; \int_{S_1}^{S_2} \sigma_{\theta\theta}(\lambda(\lambda_i,S),S)\mathrm{d}S}{S_e - 1}, \quad (5.41)$$

where S_o to S_1 is the interval where the fibres are being recruited and S_1 to S_2 is the interval where the fibres are fully recruited.

5.1.8. Radial stress

The equations of equilibrium in spherical coordinates are given by

$$\frac{\partial \sigma_{rr}}{\partial r} + \frac{1}{r}\frac{\partial \sigma_{r\theta}}{\partial \theta} + \frac{1}{r\sin\theta}\frac{\partial \sigma_{r\phi}}{\partial \phi} + \frac{1}{r}(2\sigma_{rr} - \sigma_{\theta\theta} - \sigma_{\phi\phi} + \sigma_{r\theta}\cot\theta) = 0, \quad (5.42)$$

$$\frac{\partial \sigma_{r\theta}}{\partial r} + \frac{1}{r}\frac{\partial \sigma_{\theta\theta}}{\partial \theta} + \frac{1}{r\sin\theta}\frac{\partial \sigma_{\theta\phi}}{\partial \phi} + \frac{1}{r}[(\sigma_{\theta\theta} - \sigma_{\phi\phi})\cot\theta + 3\sigma_{r\theta}] = 0 \quad (5.43)$$

and

$$\frac{\partial \sigma_{r\phi}}{\partial r} + \frac{1}{r}\frac{\partial \sigma_{\theta\phi}}{\partial \theta} + \frac{1}{r\sin\theta}\frac{\partial \sigma_{\phi\phi}}{\partial \phi} + \frac{1}{r}(2\sigma_{\theta\phi}\cot\theta + 3\sigma_{r\phi}) = 0. \quad (5.44)$$

Due to the symmetry of the problem

$$\frac{\partial}{\partial \theta} = \frac{\partial}{\partial \phi} = 0, \quad (5.45)$$

$$\sigma_{\theta\theta} = \sigma_{\phi\phi} \quad (5.46)$$

and

$$\sigma_{r\theta} = \sigma_{r\phi}. \quad (5.47)$$

Thus, equations (5.42)–(5.44) reduce to

$$\frac{\partial \sigma_{rr}}{\partial r} + \frac{1}{r}(2\sigma_{rr} - 2\sigma_{\theta\theta} + \sigma_{r\theta}\cot\theta) = 0, \quad (5.48)$$

$$\frac{\partial \sigma_{r\theta}}{\partial r} + \frac{3\sigma_{r\theta}}{r} = 0 \quad (5.49)$$

and

$$\frac{\partial \sigma_{r\phi}}{\partial r} + \frac{1}{r}(2\sigma_{\theta\phi}\cot\theta + 3\sigma_{r\phi}) = 0. \quad (5.50)$$

Due again to symmetry and comparing equation (5.49) with equation (5.50), we find that $\sigma_{\theta\phi} = 0$. By employing equation (5.6), we can write r as $r = R_i(S^3 + \lambda_i^3 - 1)^{1/3}$, from which $\mathrm{d}r = R_i(S^2/(S^3 + \lambda_i^3 - 1)^{2/3})\,\mathrm{d}S$. Using this expression together with the relation $R = R_iS$, equation (5.49) can be rewritten as

$$\frac{\partial \sigma_{r\theta}}{\sigma_{r\theta}} + 3\frac{S^2}{S^3 + \lambda_i^3 - 1}\mathrm{d}S = 0, \quad (5.51)$$

the solution of which is given by

$$\sigma_{r\theta}(\lambda_i,S) = \frac{C}{S^3 + \lambda_i^3 - 1}, \quad (5.52)$$

where C is an arbitrary constant. Since $\sigma_{r\theta}(\lambda_i = 1) = 0$ for any S, $C = 0$ and hence $\sigma_{r\theta} = 0$. Thus, the shear stresses are zero in the sphere wall. In a similar fashion, equation (5.48) can be written as:

$$\frac{\partial \sigma_{rr}}{\partial S} + 2\frac{S^2}{S^3 + \lambda_i^3 - 1}\sigma_{rr} = 2\frac{S^2}{S^3 + \lambda_i^3 - 1}\sigma_{\theta\theta}(\lambda_i,S). \quad (5.53)$$

To obtain the solution, first multiply both sides by $(S^3 + \lambda_i^3 - 1)^{2/3}$:

$$\frac{\partial \sigma_{rr}}{\partial S}(S^3 + \lambda_i^3 - 1)^{2/3} + 2\frac{S^2}{(S^3 + \lambda_i^3 - 1)^{1/3}}\sigma_{rr} = 2\frac{S^2}{(S^3 + \lambda_i^3 - 1)^{1/3}}\sigma_{\theta\theta}(\lambda_i,S), \quad (5.54)$$

rearranging the left-hand side as the differential of the product of two terms σ_{rr} and $(S^3 + \lambda_i^3 - 1)^{2/3}$

$$\frac{\partial[\sigma_{rr}(S^3 + \lambda_i^3 - 1)^{2/3}]}{\partial S} = 2\frac{S^2}{(S^3 + \lambda_i^3 - 1)^{1/3}}\sigma_{\theta\theta}(\lambda_i,S) \quad (5.55)$$

the final solution is obtained by integrating both sides with ∂S

$$\sigma_{rr}(\lambda_i,S) = \frac{2}{(S^3 + \lambda_i^3 - 1)^{2/3}}\int_1^{S_e}\frac{S^2}{(S^3 + \lambda_i^3 - 1)^{1/3}}\sigma_{\theta\theta}(\lambda_i,S)\,\mathrm{d}S. \quad (5.56)$$

The mean radial stress ($\bar{\sigma}_{rr}$) as a function of the stretch ratio at the inner surface is calculated as

$$\bar{\sigma}_{rr}(\lambda_i) = \frac{\left[\int_1^{S_e}(S^2/(S^3 + \lambda_i^3 - 1)^{1/3})\sigma_{\theta\theta}(\lambda_i,S)\,\mathrm{d}S\right]\left[\int_1^{S_e}(2/(S^3 + \lambda_i^3 - 1)^{2/3})\,\mathrm{d}S\right]}{S_e - 1}. \quad (5.57)$$

5.1.9. Circumferential tension

The circumferential tension (T) at a given radius for a wavy fibre can be calculated from the circumferential stress as:

$$T_{f,\theta\theta}(\lambda_i,S) = \sigma_{f,\theta\theta}(\lambda_i,S)r = \sigma_{f,\theta\theta}(\lambda_i,S)\lambda(\lambda_i,S)R(R_i,S) \quad (5.58)$$

thus, during and after recruitment the tension can be evaluated from equations (5.19) and (5.20), respectively:

$$T_{f,\theta\theta}(\lambda_i,S,R_i) = \frac{\delta_f Y_f R_i \lambda^2}{B(\alpha,\beta)\alpha(\alpha+1)}\frac{\lambda - w_1G_o}{w_1G_o}\left(\frac{\lambda - w_1G_o}{w_2G_o - w_1G_o}\right)^{\alpha}((\alpha+1)A_1 - \alpha B_1) \quad \text{for } w_1G_o \le \lambda < w_2G_o, \quad (5.59)$$

and

$$T_{f,\theta\theta}(\lambda_i,S,R_i) = \frac{\delta_f Y_f R_i \lambda^2}{B(\alpha,\beta)\alpha(\alpha+1)}\frac{\lambda - w_1G_o}{w_1G_o}((\alpha+1)A_2 - \alpha B_2), \quad \text{for } \lambda \ge w_2G_o. \quad (5.60)$$

Similarly, the tension from the ECM contribution could be obtained from equation (5.37)

$$T_{m,\theta\theta}(\lambda_i,S,R_i) = \sigma_{m,\theta\theta}(\lambda_i,S)r = \sigma_{m,\theta\theta}(\lambda_i,S)\lambda(\lambda_i,S)R(R_i,S) = \delta_m Y_m R_i \lambda^2(\lambda - 1). \quad (5.61)$$

The total circumferential tension ($T_{\theta\theta}$) of the tissue arise from the summed combination of both the fibres and the matrix ($T_{\theta\theta} = T_{f,\theta\theta} + T_{m,\theta\theta}$).

Finally, the total circumferential tension across the wall at a given λ_i and R_i can be calculated as

$$T_{\theta\theta}(\lambda_i,R_i) = \int_{r_i}^{r_e}\sigma_{\theta\theta}(\lambda_i,S)\,\mathrm{d}r = R_i\int_1^{S_e}\sigma_{\theta\theta}\frac{S^2}{(S^3 + \lambda_i^3 - 1)^{2/3}}\mathrm{d}S. \quad (5.62)$$

5.1.10. Alveolar pressure, volume and elastance

The alveolar pressure (P_{alv}) is evaluated as

$$P_{\mathrm{alv}}(\lambda_i) = \sigma_{rr}(\lambda_i,S = 1) = \frac{2}{\lambda_i^2}\int_1^{S_e}\frac{S^2}{(S^3 + \lambda_i^3 - 1)^{1/3}}\sigma_{\theta\theta}(\lambda_i,S)\,\mathrm{d}S. \quad (5.63)$$

The change in volume (ΔV) normalized by the initial volume (V_o) for an alveolus is

$$\frac{\Delta V}{V_o} = \lambda_i^3 - 1. \quad (5.64)$$

The specific alveolar elastance E_s is defined as

$$E_s = V_o \frac{\mathrm{d}P_{\mathrm{alv}}}{\mathrm{d}V}. \tag{5.65}$$

5.1.11. Analytical approximations for a thin-sphere model

Assuming the alveolus to be a thin-walled sphere, the average circumferential stress across the wall is approximated by the stress in the middle layer, $S_m = (S_e + 1)/2$ and $\lambda_m(\lambda_i, S) = ((S_m^3 + \lambda_i^3 - 1)/S_m^3)^{1/3}$

Thus, the circumferential stress and all related quantities such as the circumferential stiffness, alveolar pressure, specific elastance and tension can be approximated from their respective thick-wall equations (equations (5.41), (5.58), (5.60) and (5.61)) as

$$\bar{\sigma}_{\theta\theta} \cong \sigma_{\theta\theta}(\lambda_i, S_m), \tag{5.66}$$

$$\bar{E}_{\theta\theta} \cong E_{\theta\theta}(\lambda_i, S_m), \tag{5.67}$$

$$P_{\mathrm{alv}}(\lambda_i) \cong \bar{\sigma}_{\theta\theta}\left[\frac{\lambda_e^2}{\lambda_i^2} S_e^2 - 1\right], \tag{5.68}$$

$$E_s \cong \frac{\bar{E}_{\theta\theta}(\lambda_i^2 \lambda_e^3 S_e^3 - \lambda_i^4 \lambda_e S_e) - \bar{\sigma}_{\theta\theta}\lambda_m^2 S_m^2 (S_e^3 - 1)}{\lambda_i^4 \lambda_e \lambda_m^2 S_e S_m^2} \tag{5.69}$$

and

$$T_{\theta\theta}(\lambda_i, R_i) \cong \bar{\sigma}_{\theta\theta} R_i \lambda_i \left(\frac{\lambda_e}{\lambda_i} S_e - 1\right). \tag{5.70}$$

Finally, relating pressure to tension

$$P_{\mathrm{alv}}(\lambda_i) \cong \frac{T_{\theta\theta}}{R_i \lambda_i ((\lambda_e/\lambda_i) S_e - 1)}\left[\frac{\lambda_e^2}{\lambda_i^2} S_e^2 - 1\right] \cong \frac{T_{\theta\theta}}{R_i \lambda_i}\left[\frac{\lambda_e}{\lambda_i} S_e + 1\right] \tag{5.71}$$

and

$$P_{\mathrm{alv}}(\lambda_i) \cong \frac{T_{\theta\theta}}{r_i}\left[\frac{\lambda_e R_e}{\lambda_i R_i} + 1\right] \cong \frac{\bar{T}_{\theta\theta}}{r_i}\left[\frac{r_e}{r_i} + 1\right] \cong 2\frac{T_{\theta\theta}(\lambda_i, R_i)}{r_i}. \tag{5.72}$$

The latter relation is consistent with the Laplace equation. However, our formulation now relates $\bar{T}_{\theta\theta}$ to the components of the alveolar wall.

5.1.12. Fibre stress distribution

To find the probability distribution of the stress $p_\sigma(\lambda)$, we use the identity

$$|p_\sigma(\lambda)\,\mathrm{d}\sigma_f| = |p_{w_f}(w_f)\,\mathrm{d}w_f|. \tag{5.73}$$

Thus, we can write

$$p_{\sigma_f}(\lambda) = p_{w_f}(w_f)\left|\frac{\mathrm{d}w_f}{\mathrm{d}\sigma_f}\right| \tag{5.74}$$

and

$$p_{\sigma_f}(\lambda) = \frac{Y_f \lambda}{S_e - 1}\frac{(Y_f\lambda - w_1 G_o(\sigma_f + Y_f))^{\alpha-1}(w_2 G_o(\sigma_f + Y_f) - Y_f\lambda)^{\beta-1}}{B(\alpha,\beta)(w_2 G_o - w_1 G_o)^{\alpha+\beta-1}(\sigma_f + Y_f)^{\alpha+\beta}}, \tag{5.75}$$

where the range of fibre stress individual fibres, maximum ($\sigma_{f,\max}$) and minimum ($\sigma_{f,\min}$), is equal to

$$\sigma_{f,\max} = Y_f\left(\frac{\lambda - w_1 G_o}{w_1 G_o}\right) \quad \text{and} \quad \sigma_{f,\min} = Y_f\left(\frac{\lambda - w_2 G_o}{w_2 G_o}\right), \quad \text{for } \lambda > w_2 G_o \tag{5.76}$$

and

$$\sigma_{f,\max} = Y_f\left(\frac{\lambda - w_1 G_o}{w_1 G_o}\right) \quad \text{and} \quad \sigma_{f,\min} = 0, \quad \text{for } w_1 G_o \le \lambda < w_2 G_o. \tag{5.77}$$

5.2. Collagen waviness

To reduce the number of parameters in data fitting, we investigated collagen waviness in lung tissue. Fresh bovine lungs (Research 87 Inc., MA, USA) were obtained and imaged on the same day. Tissue samples, with a length and width less than 1 cm and a thickness of approximately 1 mm, were prepared using a razor blade, and glued to a coverslip at the sides without inducing any tension in the tissue. The coverslip was part of a three-dimensional printed rectangular well (86 × 44 × 10 mm) that had a top opening (66 × 17.5 mm) onto which the coverslip was glued. The samples were placed in phosphate buffer solution (PBS) at room temperature. Before imaging, the PBS around the tissue was removed, the well was inverted and oil was placed on the other side of the coverslip for upright microscopy imaging. If needed, drops of PBS were added to assure the samples remained moist.

Imaging of collagen in the bovine lung samples was accomplished through SHG imaging with an upright Multiphoton Microscopy (MPM) system (Ultima Investigator, Bruker, Billerica, MA, USA) [62]. Details of the MPM system are described in detail elsewhere [63]. Briefly, the MPM system consisted of a femtosecond laser source (Spectra Physics, Insight DS+, Santa Clara, CA, USA) tuned to 1050 nm, which provided the excitation for SHG imaging. A quarter wave-plate (QWP) (AQWP05M-980, Thorlabs, Newton, NJ, USA) was placed in the illumination path, circularly polarizing the light to sample all possible collagen orientations during SHG imaging. The illumination and SHG light paths were coupled through a 60× oil-immersion objective (NA = 1.42, working distance = 0.15 mm) (Olympus, Tokyo, Japan). A photomultiplier tube (Hamamatsu Photonics, R6357, Hamamatsu City, Japan) was used to detect the SHG light through a 525/70 nm bandpass filter (Chroma, Bellows Falls, VT, USA). The field of view (FOV) was 156 × 156 µm, with a sampling resolution of 0.15 µm/pixel and a pixel dwell time between 1 and 16 µs. *Z*-stacks containing 10–30 slices were collected for each FOV with a step size between 1 and 2 µm. To reduce noise in *z*-stacks, every consecutive pair of frames was averaged. Laser power and photomultiplier tube voltage were optimized to achieve maximum signal from collagen fibres in the bovine lung samples without damaging the samples.

The individual images of each *z*-stack as well as their maximum intensities were loaded into FIJI [64]. Alveolar walls were located and zoomed into view, and the individual collagen fibres in each wall were traced manually and fitted with a spline (figure 2). Every bend in a tracing was marked by a minimum of five data points. The arc length across each outlined fibre (that is, its length neglecting the undulations due to waviness) was also traced manually and fit with a spline. The data were exported to MATLAB R2018b (MathWorks, CA, USA) to compute waviness for each fibre, defined as the fibre length over the arc length. Figure 2 shows the resulting histogram of waviness together with its best fit beta probability distribution function (equation (2.1)). This provides values for the shape parameter values α and β, and allows us to specify the range of fibre waviness ($w_2 - w_1$).

5.3. Data fitting

Fixing the values of α, β and the range $w_2 - w_1$ as described above allows the model to be fit to experimental *P–V* curves by adjusting the values of only the three remaining free parameters (Y_{ce}, Y_{ee} and w_1). The model was fit to two individual healthy adult human *P–V* curves published by Clements *et al*. [13] and Niewoehner *et al*. [14], as well as an averaged adult *P–V* curve by Verbeken *et al*. [12]. These *P–V* curves were recorded from isolated lungs that were first degassed, inflated to total lung capacity (TLC) and then deflated. All deflations reached a pressure of zero except that from Niewoehner *et al*. [14] which ended slightly above zero. To estimate the initial volume (V_o) in this case, the *P–V* data were fitted with a sigmoidal curve

which was then extrapolated to $P = 0$ [65]. We digitized these P–V relationships and performed our model fitting using the lsqcurvefit and to obtain confidence intervals using the nlparci functions in Matlab R2018b (MathWorks, CA, USA).

Several mechanisms contribute to the P–V curve [66]. To minimize the influence of recruitment and alveolar wall folding, only the deflation limb was used in the fitting. We fitted the data with and without surface tension to explore the effect of this term on the fibre-related parameters. We assumed homogeneity and isotropic expansion of all alveoli. Thus, the change in alveolar volume over the initial volume ($\Delta V/V_o$) for a single alveolus is equivalent to that of the whole lung. Assuming a quasi-steady deflation process, the pressure is homogeneous throughout the lung. Values of 1.05 and 115.24 µm were used for S_e and R_i, respectively, based on the literature [58–60] (see electronic supplementary material, for details). The Akaike criterion [67] was employed to select the best model. The fitting was done using the numerical model equations.

5.4. Analytical approximation and engineering stress

After fitting the data using the numerical model, we tested our analytical approximations against the numerical solutions. The analytical approximation assumes uniform stress distribution across the thickness while applying the conservation of mass. The analytical approximations to pressure and stress closely matched the numerical values obtained by solving the exact equations (see electronic supplementary material, for details). Furthermore, to check the range of errors introduced if alveolar wall thinning is not considered, we compared our numerical solution with that calculated using engineering stress, defined as the force per undeformed area (see electronic supplementary material for details). Since the analytical solution matched the numerical one (electronic supplementary material, figure S2), we used the analytical equations in all simulations, unless otherwise noted.

5.5. Sensitivity analysis

Each estimated baseline parameter was varied individually to investigate its effect on the P–V curve. We varied the two fibre stiffness parameters (Y_{ee} and Y_{ce}) by ±50%. S_e was varied by changing T_i/R_i by ±50%. In varying waviness parameters, the free fibre length over the arc length was changed by ±50%. For example, for a $w_1 = 1.29$, the free fibre length beyond the arc length is 0.29. If the value was reduced by 50% (0.145), then a new w_1 was assigned a value of 1.145. In varying the waviness range $dw = w_2 - w_1$, w_1 was kept fixed while the free length over the arc length of w_2 was changed by ±50%. α and β were varied such that the beta distribution became a Gaussian or a left-skewed distribution.

5.6. Alveolar inflation stability

Guided by the sensitivity analysis, we investigated whether our model exhibits inflation instability. We partition inflation instability into two distinct physiological regimes. The first regime, which we term geometric instability, begins when alveolar stiffness (change in pressure with change in volume) or, equivalently, the effective incremental bulk modulus (product of stiffness and alveolar volume) starts to decrease monotonically towards zero. The second regime manifests as a runaway phenomenon in which the stiffness and the effective incremental bulk modulus become and stay negative. Throughout the geometric instability regime, pressure continues to increase with increasing volume, albeit at a decelerating rate. In the runaway regime, volume increases rapidly while pressure decreases towards zero. Figure 5*b* exemplifies and elaborates on these definitions. We point out that in the geometric instability regime, there is no plastic deformation of the tissues. To determine how stability is influenced by critical parameters in the model, the baseline P–V curve was investigated up to higher $\Delta V/V_o$ values (approx. 200) along with five additional simulations using a smaller S_e ratio, lower Y_{ce}, no collagen ($Y_{ce} = 0$), larger dw and a truncated Gaussian waviness distribution with the same waviness range.

5.7. Multiscale analysis

After demonstrating the ability of the model to replicate physiological behaviour on a macroscopic level, we used the model to provide estimates of microscopic stresses and stiffnesses at the alveolar wall and individual fibre level. First, we computed the contribution of each fibre to both the circumferential and radial alveolar wall stress and stiffness. Then, we calculated the stresses carried by individual fibres. This analysis provides insight into how alveolar pressure generates radial stress throughout the septal wall.

Data accessibility. Model results and Matlab code will be made available upon request. The data are provided in electronic supplementary material [68].

Authors' contributions. S.B.J. designed studies, derived model, carried out simulation, collected imaging data and drafted the manuscript; K.K. carried out imaging; D.R. designed imaging; F.V. designed studies; J.H. interpreted results, carried out simulations; D.C. designed studies, interpreted results; K.R.L. designed studies, interpreted results; D.S. designed studies, contributed to model development; J.H.T.B. designed studies, interpreted results, drafted the manuscript; B.S. designed studies, contributed to theory, interpreted results, drafted the manuscript.

Competing interests. We declare we have no competing interests.

Funding. This study was supported by NIH grant no. U01 HL-139466.

References

1. Osborne WA, Sutherland W. 1909 The elasticity of rubber balloons and hollow viscera. *Proc. R. Soc. Lond. B* **81**, 485–499. (doi:10.1098/rspb.1909.0047)
2. Goriely A, Destrade M, Amar MB. 2006 Instabilities in elastomers and soft tissues. *Q. J. Mech. Appl. Math.* **59**, 615–630. (doi:10.1093/qjmam/hbl017)
3. Lanir Y. 1983 Constitutive equations for fibrous connective tissues. *J. Biomech.* **16**, 1–12. (doi:10.1016/0021-9290(83)90041-6)
4. Horowitz A, Lanir Y, Yin FC, Perl M, Sheinman I, Strumpf RK. 1988 Structural three-dimensional constitutive law for the passive myocardium. *J. Biomech. Eng.* **110**, 200–207. (doi:10.1115/1.3108431)
5. Sacks MS. 2003 Incorporation of experimentally-derived fiber orientation into a structural constitutive model for planar collagenous tissues. *J. Biomech. Eng.* **125**, 280–287. (doi:10.1115/1.1544508)
6. Decraemer WF, Maes MA, Vanhuyse VJ. 1980 An elastic stress–strain relation for soft biological tissues based on a structural model. *J. Biomech.* **13**, 463–468. (doi:10.1016/0021-9290(80)90338-3)
7. Agianniotis A, Rezakhaniha R, Stergiopulos N. 2011 A structural constitutive model considering angular dispersion and waviness of collagen fibres of rabbit facial veins. *Biomed. Eng. Online* **10**, 1–7. (doi:10.1186/1475-925X-10-18)
8. Mead J. 1961 Mechanical properties of lungs. *Physiol. Rev.* **41**, 281–330. (doi:10.1152/physrev.1961.41.2.281)
9. Maksym GN, Bates JHT. 1997 A distributed nonlinear model of lung tissue elasticity. *J. Appl. Physiol.* **82**, 32–41. (doi:10.1152/jappl.1997.82.1.32)
10. Stamenovic D, Wilson TA. 1992 Parenchymal stability. *J. Appl. Physiol.* **73**, 596–602. (doi:10.1152/jappl.1992.73.2.596)

11. Smith JC, Stamenovic D. 1986 Surface forces in lungs. I. Alveolar surface tension–lung volume relationships. *J. Appl. Physiol.* **60**, 1341–1350. (doi:10.1152/jappl.1986.60.4.1341)
12. Verbeken EK, Cauberghs M, Mertens I, Clement J, Lauweryns JM, Van de Woestijne KP. 1992 The senile lung. Comparison with normal and emphysematous lungs. 2. Functional aspects. *Chest* **101**, 800–809. (doi:10.1378/chest.101.3.800)
13. Clements JA, Hustead RF, Johnson RP, Gribetz I. 1961 Pulmonary surface tension and alveolar stability. *J. Appl. Physiol.* **16**, 444–450. (doi:10.1152/jappl.1961.16.3.444)
14. Niewoehner DE, Kleinerman J, Liotta L. 1975 Elastic behavior of postmortem human lungs: effects of aging and mild emphysema. *J. Appl. Physiol.* **39**, 943–949. (doi:10.1152/jappl.1975.39.6.943)
15. Iravani A, Thambyah A, Burrowes KS. 2020 A viscoelastic two-dimensional network model of the lung extracellular matrix. *Biomech. Model. Mechanobiol.* **19**, 2241–2253. (doi:10.1007/s10237-020-01336-1)
16. Licup AJ, Münster S, Sharma A, Sheinman M, Jawerth LM, Fabry B, Weitz DA, Mackintosh FC. 2015 Stress controls the mechanics of collagen networks. *Proc. Natl Acad. Sci. USA* **112**, 9573–9578. (doi:10.1073/pnas.1504258112)
17. Denny E, Schroter RC. 1999 Viscoelastic behavior of a lung alveolar duct model. *J. Biomech. Eng.* **122**, 143–151. (doi:10.1115/1.429644)
18. Desai LP, Chapman KE, Waters CM. 2008 Mechanical stretch decreases migration of alveolar epithelial cells through mechanisms involving Rac1 and Tiam1. *Am. J. Physiol. Lung Cell Mol. Physiol.* **295**, L958–L965. (doi:10.1152/ajplung.90218.2008)
19. Roan E, Waters CM. 2011 What do we know about mechanical strain in lung alveoli? *Am. J. Physiol. Lung Cell Mol. Physiol.* **301**, L625–L635. (doi:10.1152/ajplung.00105.2011)
20. Sobin SS, Fung YC, Tremer HM. 1988 Collagen and elastin fibers in human pulmonary alveolar walls. *J. Appl. Physiol.* **64**, 1659–1675. (doi:10.1152/jappl.1988.64.4.1659)
21. Mercer RR, Crapo JD. 1990 Spatial distribution of collagen and elastin fibers in the lungs. *J. Appl. Physiol.* **69**, 756–765. (doi:10.1152/jappl.1990.69.2.756)
22. Rezakhaniha R, Agianniotis A, Schrauwen JTC, Griffa A, Sage D, Bouten CVC, Van De Vosse FN, Unser M, Stergiopulos N. 2012 Experimental investigation of collagen waviness and orientation in the arterial adventitia using confocal laser scanning microscopy. *Biomech. Model. Mechanobiol.* **11**, 461–473. (doi:10.1007/s10237-011-0325-z)
23. Guthold M, Liu W, Sparks EA, Jawerth LM, Peng L, Falvo M, Superfine R, Hantgan RR, Lord ST. 2007 A comparison of the mechanical and structural properties of fibrin fibers with other protein fibers. *Cell Biochem. Biophys.* **49**, 165–181. (doi:10.1007/s12013-007-9001-4)
24. Yi E, Sato S, Takahashi A, Parameswaran H, Blute TA, Bartolák-Suki E, Suki B. 2016 Mechanical forces accelerate collagen digestion by bacterial collagenase in lung tissue strips. *Front. Physiol.* **7**, 287. (doi:10.3389/fphys.2016.00287)
25. Sherratt MJ, Baldock C, Haston JL, Holmes DF, Jones CJP, Shuttleworth CA, Wess TJ, Kielty CM. 2003 Fibrillin microfibrils are stiff reinforcing fibres in compliant tissues. *J. Mol. Biol.* **332**, 183–193.
26. Dutov P, Antipova O, Varma S, Orgel JPRO, Schieber JD. 2016 Measurement of elastic modulus of collagen type I single fiber. *PLoS ONE* **11**, e0145711. (doi:10.1371/journal.pone.0145711)
27. Fung YC. 1993 *Biomechanics: mechanical properties of living tissues*, 2nd edn. New York, NY: Springer-Verlag.
28. Sherebrin MH, Song SH, Roach MR. 1983 Mechanical anisotropy of purified elastin from the thoracic aorta of dog and sheep. *Can. J. Physiol. Pharmacol.* **61**, 539–545.
29. Jorba I, Beltrán G, Falcones B, Suki B, Farré R, García-Aznar JM, Navajas D. 2019 Nonlinear elasticity of the lung extracellular microenvironment is regulated by macroscale tissue strain. *Acta Biomater.* **92**, 265–276. (doi:10.1016/j.actbio.2019.05.023)
30. Knudsen L, Lopez-Rodriguez E, Berndt L, Steffen L, Ruppert C, Bates JHT, Ochs M, Smith BJ. 2018 Alveolar micromechanics in bleomycin-induced lung injury. *Am. J. Respir. Cell Mol. Biol.* **59**, 757–769. (doi:10.1165/rcmb.2018-0044OC)
31. Stamenovic D, Smith JC. 1986 Surface forces in lungs. II. Microstructural mechanics and lung stability. *J. Appl. Physiol.* **60**, 1351–1357. (doi:10.1152/jappl.1986.60.4.1351)
32. Bachofen H, Schürch S. 2001 Alveolar surface forces and lung architecture. *Comp. Biochem. Physiol. A Mol. Integr. Physiol.* **129**, 183–193. (doi:10.1016/S1095-6433(01)00315-4)
33. Maina JN, West JB. 2005 Thin and strong! The bioengineering dilemma in the structural and functional design of the blood-gas barrier. *Physiol. Rev.* **85**, 811–844. (doi:10.1152/physrev.00022.2004)
34. Alexander H. 1971 Tensile instability of initially spherical balloons. *Int. J. Eng. Sci.* **9**, 151–160. (doi:10.1016/0020-7225(71)90017-6)
35. Xin-chun S. 1991 Tensile instability of nonlinear spherical membrane with large deformation. *Appl. Math. Mech.* **12**, 993–1000. (doi:10.1007/BF02451485)
36. Mercer RR, Laco JM, Crapo JD. 1987 Three-dimensional reconstruction of alveoli in the rat lung for pressure–volume relationships. *J. Appl. Physiol.* **62**, 1480–1487. (doi:10.1152/jappl.1987.62.4.1480)
37. Wilson TA, Bachofen H. 1982 A model for mechanical structure of the alveolar duct. *J. Appl. Physiol.* **52**, 1064–1070. (doi:10.1152/jappl.1982.52.4.1064)
38. Schürch S, Goerke J, Clements JA. 1976 Direct determination of surface tension in the lung. *Proc. Natl Acad. Sci. USA* **73**, 4698–4702. (doi:10.1073/pnas.73.12.4698)
39. Bachofen H, Hildebrandt J, Bachofen M. 1970 Pressure–volume curves of air- and liquid-filled excised lungs-surface tension in situ. *J. Appl. Physiol.* **29**, 422–431. (doi:10.1152/jappl.1970.29.4.422)
40. Alencar AM, Arold SP, Buldyrev SV, Majumdar A, Stamenović D, Stanley HE, Suki B. 2002 Physiology: dynamic instabilities in the inflating lung. *Nature* **417**, 809–811. (doi:10.1038/417809b)
41. Gehr P, Bachofen M, Weibel ER. 1978 The normal human lung: ultrastructure and morphometric estimation of diffusion capacity. *Respir. Physiol.* **32**, 121–140. (doi:10.1016/0034-5687(78)90104-4)
42. West JB, Tsukimoto K, Mathieu-Costello O, Prediletto R. 1991 Stress failure in pulmonary capillaries. *J. Appl. Physiol.* **70**, 1731–1742. (doi:10.1152/jappl.1991.70.4.1731)
43. Kononov S, Brewer K, Sakai H, Cavalcante FS, Sabayanagam CR, Ingenito EP, Suki B. 2001 Roles of mechanical forces and collagen failure in the development of elastase-induced emphysema. *Am. J. Respir. Crit. Care Med.* **164**, 1920–1926. (doi:10.1164/ajrccm.164.10.2101083)
44. D'Errico A, Scarani P, Colosimo E, Spina M, Grigioni WF, Mancini AM. 1989 Changes in the alveolar connective tissue of the ageing lung: an immunohistochemical study. *Virchows Arch. A Pathol. Anat. Histopathol.* **415**, 137–144. (doi:10.1007/BF00784351)
45. Michel R, Zwikler M, Bates JHT. 1993 Effect of severe experimental fibrosis on lung resistance and elastance. *Am. Rev. Respir. Dis.* **147**, A595.
46. O'Donnell MD, O'Connor CM, FitzGerald MX, Lungarella G, Cavarra E, Martorana PA. 1999 Ultrastructure of lung elastin and collagen in mouse models of spontaneous emphysema. *Matrix Biol.* **18**, 357–360. (doi:10.1016/S0945-053X(99)00031-1)
47. Yuan H, Kononov S, Cavalcante FSA, Lutchen KR, Ingenito EP, Suki B. 2000 Effects of collagenase and elastase on the mechanical properties of lung tissue strips. *J. Appl. Physiol.* **89**, 3–14. (doi:10.1152/jappl.2000.89.1.3)
48. Lum H, Mitzner W. 1987 A species comparison of alveolar size and surface forces. *J. Appl. Physiol.* **62**, 1865–1871. (doi:10.1152/jappl.1987.62.5.1865)
49. Yamamoto N. 2017 Tensile strength of single collagen fibrils isolated from tendons. *Eur. J. Biophys.* **5**, 1. (doi:10.11648/j.ejb.20170501.11)
50. Shen ZL, Dodge MR, Kahn H, Ballarini R, Eppell SJ. 2008 Stress–strain experiments on individual collagen fibrils. *Biophys. J.* **95**, 3956–3963. (doi:10.1529/biophysj.107.124602)
51. Prange HD. 2003 Laplace's law and the alveolus: a misconception of anatomy and a misapplication of physics. *Adv. Physiol. Educ.* **27**, 34–40. (doi:10.1152/advan.00024.2002)
52. Knudsen L, Ochs M. 2018 The micromechanics of lung alveoli: structure and function of surfactant and tissue components. *Histochem. Cell Biol.* **150**, 661–676. (doi:10.1007/s00418-018-1747-9)
53. Matsuda M, Fung YC, Sobin SS. 1987 Collagen and elastin fibers in human pulmonary alveolar mouths and ducts. *J. Appl. Physiol.* **63**, 1185–1194. (doi:10.1152/jappl.1987.63.3.1185)

54. Kowe R, Schroter RC, Matthews FL, Hitchings D. 1986 Analysis of elastic and surface tension effects in the lung alveolus using finite element methods. *J. Biomech.* **19**, 541–549. (doi:10.1016/0021-9290(86)90127-2)
55. Fung YC. 1988 A model of the lung structure and its validation. *J. Appl. Physiol. (Bethesda Md 1985)* **64**, 2132–2141. (doi:10.1152/jappl.1988.64.5.2132)
56. Mijailovich SM, Stamenovic D, Fredberg JJ. 1993 Toward a kinetic theory of connective tissue micromechanics. *J. Appl. Physiol.* **74**, 665–681. (doi:10.1152/jappl.1993.74.2.665)
57. Mead JW, Takishima T, Leith DD. 1970 Stress distribution in lungs: a model of pulmonary elasticity. *J. Appl. Physiol.* **28**, 596–608. (doi:10.1152/jappl.1970.28.5.596)
58. Mercer RR, Russell ML, Crapo JD. 1994 Alveolar septal structure in different species. *J. Appl. Physiol. (Bethesda Md 1985)* **77**, 1060–1066. (doi:10.1152/jappl.1994.77.3.1060)
59. Dawson TH. 2003 Scaling laws for capillary vessels of mammals at rest and in exercise. *Proc. R. Soc. Lond. B* **270**, 755–763. (doi:10.1098/rspb.2002.2304)
60. Dawson TH. 2014 Allometric relations and scaling laws for the cardiovascular system of mammals. *Systems* **2**, 168–185. (doi:10.3390/systems2020168)
61. Wuyts FL, Vanhuyse VJ, Langewouters GJ, Decraemer WF, Raman ER, Buyle S. 1995 Elastic properties of human aortas in relation to age and atherosclerosis: a structural model. *Phys. Med. Biol.* **40**, 1577–1597. (doi:10.1088/0031-9155/40/10/002)
62. Chen X, Nadiarynkh O, Plotnikov S, Campagnola PJ. 2012 Second harmonic generation microscopy for quantitative analysis of collagen fibrillar structure. *Nat. Protoc.* **7**, 654–669. (doi:10.1038/nprot.2012.009)
63. Karrobi K, Tank A, Tabassum S, Pera V, Roblyer D Diffuse and nonlinear imaging of multiscale vascular parameters for *in vivo* monitoring of preclinical mammary tumors. *J. Biophotonics* **12**, e201800379. (doi:10.1002/jbio.201800379)
64. Schindelin J *et al*. 2012 Fiji: an open-source platform for biological-image analysis. *Nat. Methods* **9**, 676–682. (doi:10.1038/nmeth.2019)
65. Venegas JG, Harris RS, Simon BA. 1998 A comprehensive equation for the pulmonary pressure–volume curve. *J. Appl. Physiol.* **84**, 389–395. (doi:10.1152/jappl.1998.84.1.389)
66. Gil J, Bachofen H, Gehr P, Weibel ER. 1979 Alveolar volume–surface area relation in air- and saline-filled lungs fixed by vascular perfusion. *J. Appl. Physiol.* **47**, 990–1001. (doi:10.1152/jappl.1979.47.5.990)
67. Bates JHT. 2009 Lung mechanics by Jason H. T. Bates. *Camb. Core*. (doi:10.1017/CBO9780511627156)
68. Jawde SB *et al*. 2021 Inflation instability in the lung: an analytical model of a thick-walled alveolus with wavy fibres under large deformations. Figshare.